

Study of the Photon Transfer Curve in the CCD detectors of the Vera C. Rubin Observatory

Lina Marcela Giraldo-Murillo^{a*}

Advisors: Andrés A. Plazas Malagón^b & Craig Lage^c

^aInstituto de Física, Universidad de Antioquia, Medellín, Colombia

^b SLAC National Accelerator Laboratory, 2575 Sand Hill Rd, Menlo Park, CA, 94025, USA

Kavli Institute for Particle Astrophysics & Cosmology, P.O. Box 2450, Stanford University, Stanford, California 94305, USA

Department of Astrophysical Sciences, Peyton Hall, Princeton University, Princeton, NJ 08544, USA

^cDepartment of Physics, University of California, Davis, USA

* lina.giraldom@udea.edu.co

October 9, 2022

Abstract

The RECA internship program allows Colombian students to get better research skills in Astronomy, Astrophysics, and Cosmology. For three months, we developed our work in this internship program, and its main objective was to study the photon transfer curves (PTC) of the Vera C. Rubin Observatory, mainly gain, and to make comparisons with the gain obtained through pairs of flats.

We used run 13144 to construct the PTCs and 13186 to analyze the crosstalk. We use *DM stack*, which is the software in development for this observatory, and it makes all the reductions for the construction of the PTCs. Also, we implement simulations to reproduce the observed effects.

We initially found a 5 % difference between the gain by PTC and pairs of flats in a range of flows between 5000 and 10000 ADU. Simulations showed that this difference was a product of the handling of the statistics and the erroneous assumption that the distribution following the Lupton equation is Gaussian. By vendor, we found an error interval for this flow region, for E2V of $(1.8 \pm 0.7, 4.1 \pm 0.9)$ % and for ITL of $(0.85 \pm 0.7, 2.2 \pm 0.9)$ %. Also, from the PTC we found the average Full Well Capacity of LSSTCam is 130000 ± 10000 e⁻.

We obtained a list of segments where we found differences with the results obtained by SLAC National Acceleration Laboratory in PTC parameters, low saturation level, or other defects. We detected and corrected the effect of statistics in the gain calculation using pairs of flats. Then, we proposed a code change for it, which was implemented in *DM stack*. In addition, we do not recommend correcting for crosstalk since it does not significantly affect the parameters and does not change the shape of the PTC; the opposite is true for the nonlinearity correction.

Keywords— PTC; Gain; Crosstalk; Linearity, Brighter Fatter effect, Full Well Capacity

1 Introduction

The Vera C. Rubin Observatory is located at Cerro Pachón in the Atacama Desert in Chile. It was chosen after considering different sites worldwide according to their meteorological conditions. It will operate the

8.4-meter Simonyi Research Telescope, which will be able to scan the entire southern sky in approximately three nights and is expected to start operations in 2024. This observatory also has the giant camera ever built, the LSST Camera, which has a 3.2 gigapixel resolution for the entire focal plane, with a diameter of 64 cm to cover 9.6 deg² FoV and a plate scale of 0.2 " pixel⁻¹ (LSST Science Collaboration et al., 2009).

This observatory is named in honor of the astronomer Vera Rubin (NSF, 2020), who in 1970 pioneered the measurement of the rotation curves of disk galaxies (Rubin, 2011), in which she realized that for the stars in galaxies to rotate at the rate they do, there must be more mass than we observe for the galaxies not to break apart. This mass is what we now call dark matter, which is one of the scientific goals of this observatory.

Vera Rubin received several awards, including the National Medal of Science, and even a ridge on Mars is named after her (Koren, 2020). In addition, she worked hard for the recognition of the work of women in science and her students (Rubin, 2011).

1.1 LSST Scientific goals

The LSST has four main scientific objectives (Ivezić et al., 2019; LSST Science Collaboration et al., 2009):

- Taking an Inventory of the Solar System: The minor bodies of the solar system, such as TNOs, asteroids, and comets, are crucial to understanding planetary formation and evolution since their orbital elements and sizes preserve this history. On the other hand, the interaction of objects in the Main Asteroid Belt, which lies between Mars and Jupiter, could launch some of these objects into Earth's orbit, so their study will help to make a connection between NEOs coming from the Main Belt.
- Mapping the Milky Way: It concerns the study of the formation and evolution of our galaxy by observing its stars' structure, dynamics, and chemical composition. In addition, this science objective will characterize the stars in the solar neighborhood (300 pc).
- Exploring the Transient Optical Sky: This time domain science observes transient and variable phenomena such as supernovae, variable stars, and AGN. The goal is to detect transient and distant objects. This requires several properties: covering a large part of the sky to increase the probability of seeing these events, good quality images to observe the differences between images, good sampling time to detect the different types of variable stars, accurate color information for classification, long-term persistent observations to follow up the event, reduction, classification and rapid publication to the community to allow the study of these objects in other fields, such as spectroscopy.
- Probing Dark Energy and Dark Matter: Dark energy affects the universe's expansion as the accumulation of mass, so the observations must depend on the redshift to study it. For this purpose, they will study weak gravitational lensing, large-scale structures such as galaxy clusters, BAO (Baryonic AcoAcousticillation), and Supernova systems, among others. For the study of dark matter, there are several mechanisms to explore it, such as weak and strong lensing of galaxy mass distributions..

1.2 What kind of CCD does the LSST Camera have?

The LSSTCam is composed of *thick fully depleted* and back-illuminated CCDs(LSST Science Collaboration et al., 2009). This type of CCD is characterized by a good response in the near-infrared regions (Lage,

Bradshaw, & Tyson, 2017), which allows observation of distant objects reddened by the universe's expansion. However, being thick, they present some effects due to the long path that the generated electrons must travel to the charge storage well.

The LSSTCam is highly segmented, which enables it to be read out completely in 2 s and reduces the readout noise produced by high readout speeds (LSST Science Collaboration et al., 2009). It comprises a mosaic of 205 CCDs organized by 21 science modules, each containing nine CCDs and four specialized corner modules for telescope guidance and alignment by active optics (Snyder et al., 2020). This mosaic has CCDs from two vendors: Imaging Technology Laboratories (ITL) and Teledyne e2v (E2V), and each is divided into 16 segments. Figure 1 shows in yellow the vendor's E2V detectors, in greenish blue the ITL detectors, which are the science CCDs, and in purple the guidance CCDs.

According to Walter (2015) for the LSST science objective in weak lensing, where the aim is to measure how this modifies the shape of galaxies by observing a wide field, it is crucial to quantify the brighter-fatter (BF, hereafter) effect since exact measurements of the PSF of galaxies are required. The BF effect leads to the deformation of the PSF, being more critical in bright objects and progressively decreasing in fainter objects (Lage et al., 2017). On the other hand, Walter (2015) mentions that another effect suffered by the sensors is the edge effect, where electrons near the edge of the sensor feel a force that pushes them inward, which mainly affects astrometry.

1.3 What is Photon Transfer Curve (PTC)?

The Photon Transfer Curve (PTC) allows the characterization of the fundamental parameters of the CCD, mainly the determination of the relationship between the electrons recorded by each pixel and their conversion to analog-to-digital counts (ADU), i.e., the gain; it also measures the nonlinearity of the camera and its Full Well Capacity (FWC). The first parameter is essential because other vital parameters, such as read noise, quantum efficiency, dark current, among others, depend on it (Downing, Baade, Sinclair, Deiries, & Christen, 2006).

Figure 2 shows the PTC of segment C06 of sensor 22 of the LSSTCam, where it is evident that at low fluxes, the variance is low and increases with the flux but not linearly until the saturation point or FWC, which for this detector is 83000 ADU. After this point, the variance begins to decrease, indicating that the flux stored in each pixel of this amplifier begins to homogenize. The nonlinear behavior of this curve is exhibited by *thick fully-depleted CCDs*, according to Downing et al. (2006) charge storage in a pixel is the main reason, since the expected relationship between the variance and the mean number of counts in a pixel is modified in flat images (Walter, 2015). The effective area of the pixel changes with the amount of charge, decreasing the more significant the charge accumulated in the pixel. Consequently, very bright sources are mainly affected by this so-called BF effect. If the pixels of the CCD segment were independent, they could be described by Poisson statistics, and the PTC would follow the green line in the figure.

1.3.1 Brighter father effect

As mentioned above, the charge stored in a pixel modifies the effective area of the pixel, decreasing the probability that this pixel will continue to store the charge. Consequently, the electrons that should have been kept in this pixel are deflected horizontally, causing more elliptical images. Thus, a process initially described by a Poisson statistic, and the charge stored in each pixel was independent of the other, breaks down by modifying the relationship between the variance and the mean number of counts per pixel (Walter,

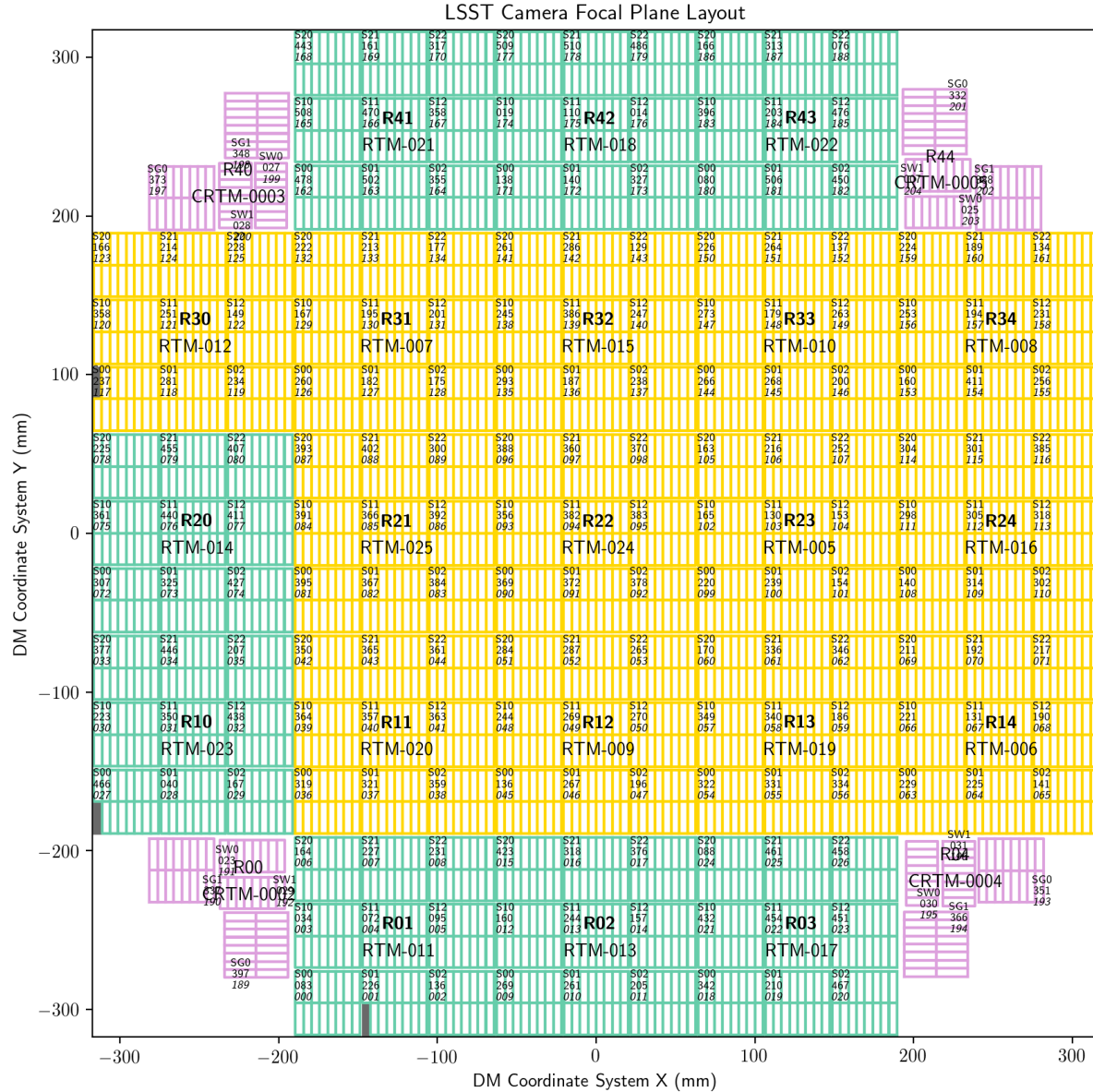


Figure 1: The focal plane of the LSST camera. The vendor's CCDs' location is blue for ITL and yellow for E2V. Each CCD (a small square) is composed of 16 segments, each with its amplifier, and 189 CCDs are responsible for taking the science data. The CCDs at the corners are for focusing and synchronization with the Earth's rotation (see LSST-SLACLab)

2015). This effect changes the PSF, so it is a potential problem in surveys interested in the variation of the brightness and shape of objects (Coulton, Armstrong, Smith, Lupton, & Spergel, 2018)

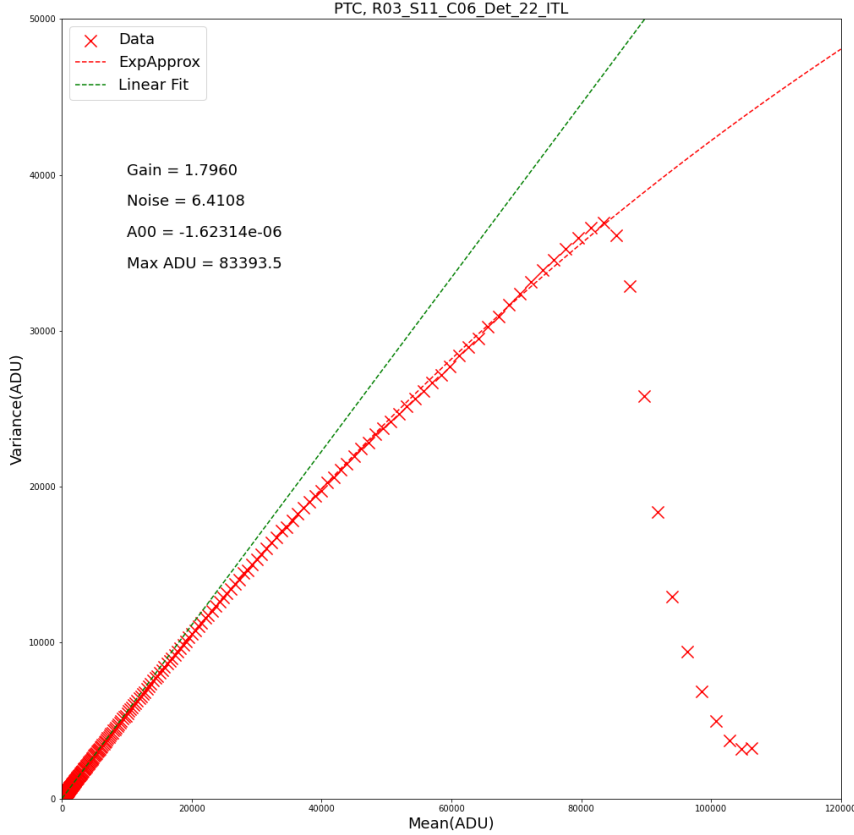


Figure 2: PTC for detector 22 was found in raft 03, sensor 11, and amplifier C06; its vendor is ITL. In red crosses, the data are shown, the red line uses the EXPAPPROXIMATION fit, and the green line is a linear fit. This curve was constructed with the results obtained via *DM stack*.

This work was developed during the RECA (Red de Estudiantes Colombiana de Astronomía) internship program 2022¹. The program was carried out over three months, in which we also developed other activities such as remote astronomical observations with the Teide Observatory².

In this report, we present the data used in the section 2. The section 3 describes the methodology used. In the section 4, we present the results and analysis. Finally, the conclusion in section 5.

2 Data

Los datos utilizados en este trabajo fueron obtenidos mediante el banco de pruebas Bench for Optical Testing (BOT), que fue construido y diseñado en SLAC National Accelerator Laboratory, el cual permite

¹RECA internship program is a training program in scientific research in Astronomy, Astrophysics, and Cosmology directed to students of Colombian institutions. The program website <https://recaastronomia.github.io/internship/>

²<https://www.iac.es/es/observatorios-de-canarias/observatorio-del-teide>

realizar pruebas de laboratorio con la LSSTCam con variaciones menores a 5% en imágenes flat de modo que puedan efectuarse medidas de la linealidad, full well y la ganancia de las PTC (Newbry et al., 2018). En la figura 3 se muestra la estructura del BOT, donde en la parte superior circular va el criostato y el plano focal queda apuntando hacia abajo del banco de pruebas.

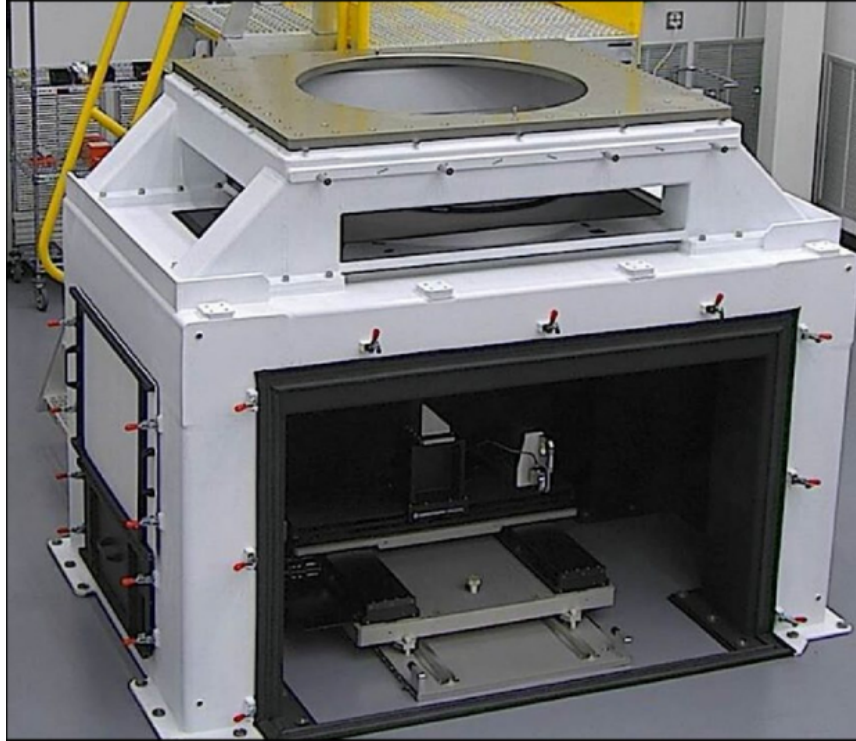


Figure 3: Banco de pruebas BOT diseñado por SLAC. Figure is taken from Newbry et al. (2018).

Se hizo uso de los *run 13144* y *run 13186*, siendo este último el que contiene la información de la matriz de crosstalk. De acuerdo con Snyder et al. (2020) las mediciones del crosstalk electrónico es llevado a cabo mediante un proyector llamado *projector crosstalk*, el cual ilumina un solo sensor con un patrón de grandes puntos brillantes con un haz de luz colimado, que posee un radio de 80 píxeles. Sin embargo, para hacer las pruebas de laboratorio simulando tamaños de fuentes reales se utiliza el proyector óptico llamado *the spot grid projector*, que genera puntos en grids específicos y cuenta con filtros que simulan tanto líneas dejadas por satélites, como el nivel de señal del fondo del cielo.

3 Methodology

The images used contain standard *overscan*, *bias*, *dark*, and *defects* reduction, which consist of maps indicating regions with both bright and dark defects, eg. dead pixels. The above reduction corresponds to the starting state for the PTC study. Subsequently, other corrections such as *linearity* and *crosstalk* are made to analyze their effects on the main parameters of the camera.

Professor Craig Lage generated supercalibrations for the entire focal plane, which are in a chain in his personal collection [u/cslage/calib/13144/calib.20220103](https://github.com/cslage/calib/13144/calib.20220103). Whereas, the images shown in Figures 4 and 5 are superbias and superdark (left panel E2V and right panel ITL), respectively, which were generated as part of the learning process for producing the calibration images using the software developed for the LSST, called *DM stack*.

The code with which the calibration images are generated via *DM stack* can be found in https://github.com/lsst/cp_pipe, and it generates the data for the construction of the PTC, calculates the gain for each CCD segment as its FWC. In addition, it calculates the gain by another different method, which was analyzed in section 3.2 to determine the differences between it and the PTC, which consists of using two pairs of flats for its estimation. We use two code versions of the *DM stack*³, for the entire focal plane:

- w_2022_27: Initial version we started working with.
- w_2022_32: Version that couples one of our main results on obtaining the gain with pairs of flats (see the DM-35790 ticket in Jira).

BPS (Batch Processing Service) was used to run the two previous versions. The details of how to build the configuration files, possible errors, associated link for more information, and how to use the obtained data can be found in the GitHub repository of this project RECA_Internship_Project in the notebook BPS_LSST.ipynb. In addition, all notebooks used to carry out the methodology described below are available in this repository. There is also a notebook called Tutorial.ipynb where I explain a little bit about the *Data Butler*, which is the API that manages and stores the data, where to find more information about it, what are the collections, visualize images, get the data and work with them, among other details about the calibration images.

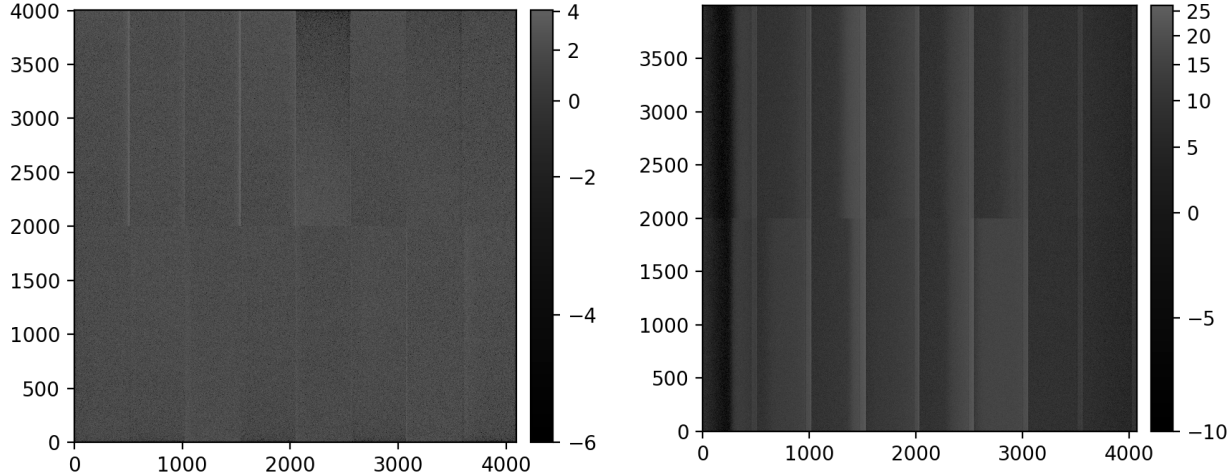


Figure 4: Masterbias for detectors 55 (E2V), on the left and 74 (ITL), on the right.

³DM stack is the software developed for the LSST and is publicly available on GitHub, and it can be found at <https://github.com/lsst/>

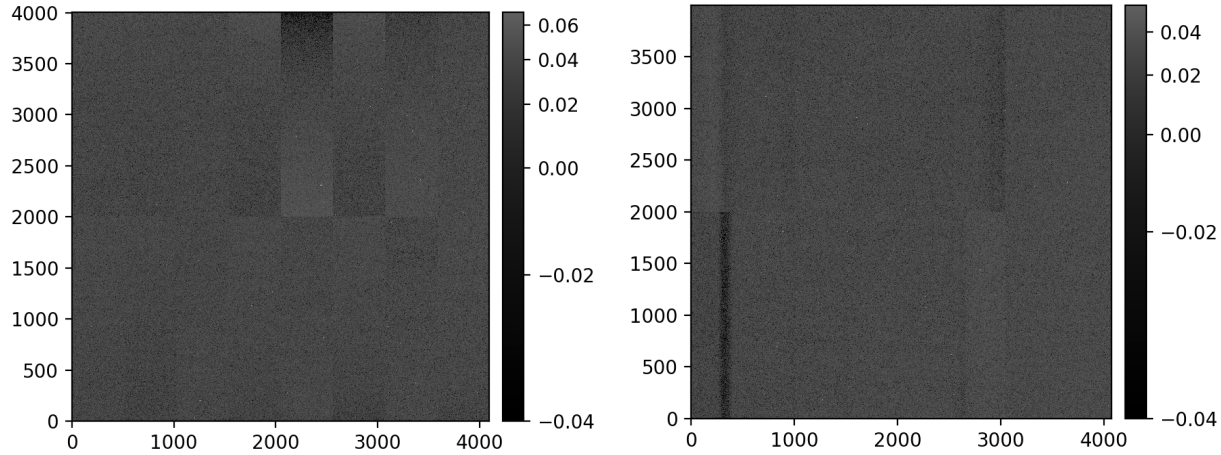


Figure 5: Masterdarks for detectors 55 (E2V), on the left and 74 (ITL), on the right.

3.1 Photon Transfer Curve (PTC)

The PTCs were generated for the whole LSSTCam focal plane using *DM stack*⁴, which allows estimating the gain, the read noise, a_{00} (parameter related to the B-F effect) and the turnoff (associated with the Full Well Capacity, FWC) from a fit to the shape of the PTC. This code implements equations 16 and 20 of the Astier et al. (2019) article: equation 16 corresponds to the exponential approximation (EXPAPPROXIMATION), which uses only the variance (C_{00}); while equation 20 is the full model (FULLCOVARIANCE), and implements the covariance matrix. In this work, we used EXPAPPROXIMATION, whose equation is as follows

$$C_{00} = \frac{1}{2g^2 a_{00}} [\exp(2a_{00}\mu g) - 1] + \frac{n_{00}}{g^2} \quad (1)$$

where C_{00} is the variance, g is the gain, a_{00} is always negative and is related to the B-F effect, μ is the mean, and n_{00} (e^l) is the noise. According to Astier et al. (2019), a_{00} being negative leads to the variance of a flat field not growing as fast as the mean does. In the case where there is no B-F effect, i.e., each pixel is independent of the other and is described by a Poisson statistic, the mean, gain, and variance are directly related through

$$V = \frac{\mu}{g} \quad (2)$$

where V is the variance of a flat field, μ is the mean, and g is the gain.

3.2 Gain from flat pairs

An independent method for calculating a sensor's gain is using flat field pairs with equal exposure times. Since each CCD is composed of 16 segments, each with its amplifier, a gain value is obtained for each

⁴The PTCs are constructed with the code available in the repository cp-pipe

segment. For this purpose, the LSST has the function Gain from flat pairs, which was analyzed in detail in this work.

We aim to quantify the difference between the gain calculated from the fit to the PTC and this method. For this, we initially calculate the average flux in ADU with each flat pair, the read noise, and the gain. The latter is estimated employing the equation of Lupton (2014)

$$\frac{1}{g} = \left\langle \frac{(I_1 - I_2)^2}{I_1 + I_2} \right\rangle \quad (3)$$

Where g is the gain, I_1 is the first flat image, and I_2 is the second flat image, both at the same exposure time. The expected value over all pixels is the inverse of gain. Considering the corrections for read-out noise, the equation takes the following quadratic form:

$$\frac{1}{g} = \left\langle \frac{(I_1 - I_2)^2}{I_1 + I_2} \right\rangle - \frac{1}{\mu} (N^2 - \frac{1}{2} g^2) \quad (4)$$

where $\mu u = 0.5(\mu_1 + \mu_2)$ with μu_1 and μu_2 the average value for each of the flat images and N is the read-out noise. This above equation has three variants: NONE, SIMPLE and FULL, with NONE being equal to the equation 3. The remaining two cases are as follows:

$$g = \begin{cases} \frac{1}{K - \frac{1}{\mu} (N^2 - \frac{1}{2} g^2)} & \text{SIMPLE} \\ \frac{\mu + \sqrt{\mu^2 - 2\mu K + 2N^2}}{2K\mu - 2K^2} & \text{FULL} \end{cases} \quad (5)$$

where K is equal to the equation 3. In the SIMPLE case $g = 1/K$, while in the FULL case the quadratic equation is solved and the result is taken to have physical meaning. Once we have the gains calculated from pairs of flats for flows between 0 and ~ 10000 ADU, we calculated the relative percentage error with the gain obtained with the fit to the PTC. We use the equation 5 with FULL type correction to calculate this relative error, thus:

$$\text{Relative_error}[\%] = \frac{|gain_{PTC} - gain_{flats}|}{gain_{PTC}} \times 100\% \quad (6)$$

Subsequently, a linear low-flow fit was performed, which we considered being between 5000 and 10000 ADU. The low-flow fit has the following form:

$$\text{Relative_error}_{LF}[\%] = mF + offset \quad (7)$$

where m is the slope of the fit, F is the flux, and $offset$ is the intercept with the y -axis. These parameters serve us to quantify the error variation in this flow range and the base error between the PTC gain and that calculated with the flats. We made histograms of these parameters to see the vendor's behavior and extract a general behavior. This is calculated by leaving out the outliers, i.e., the CCD segments with abnormal behavior. To do this, we made use of Astropy Collaboration et al. (2018) and its functions *sigma_clip* and *sigma_clipped_stats* with which we cut the data so that those that were within 3σ of the median were kept and we iterated three times.

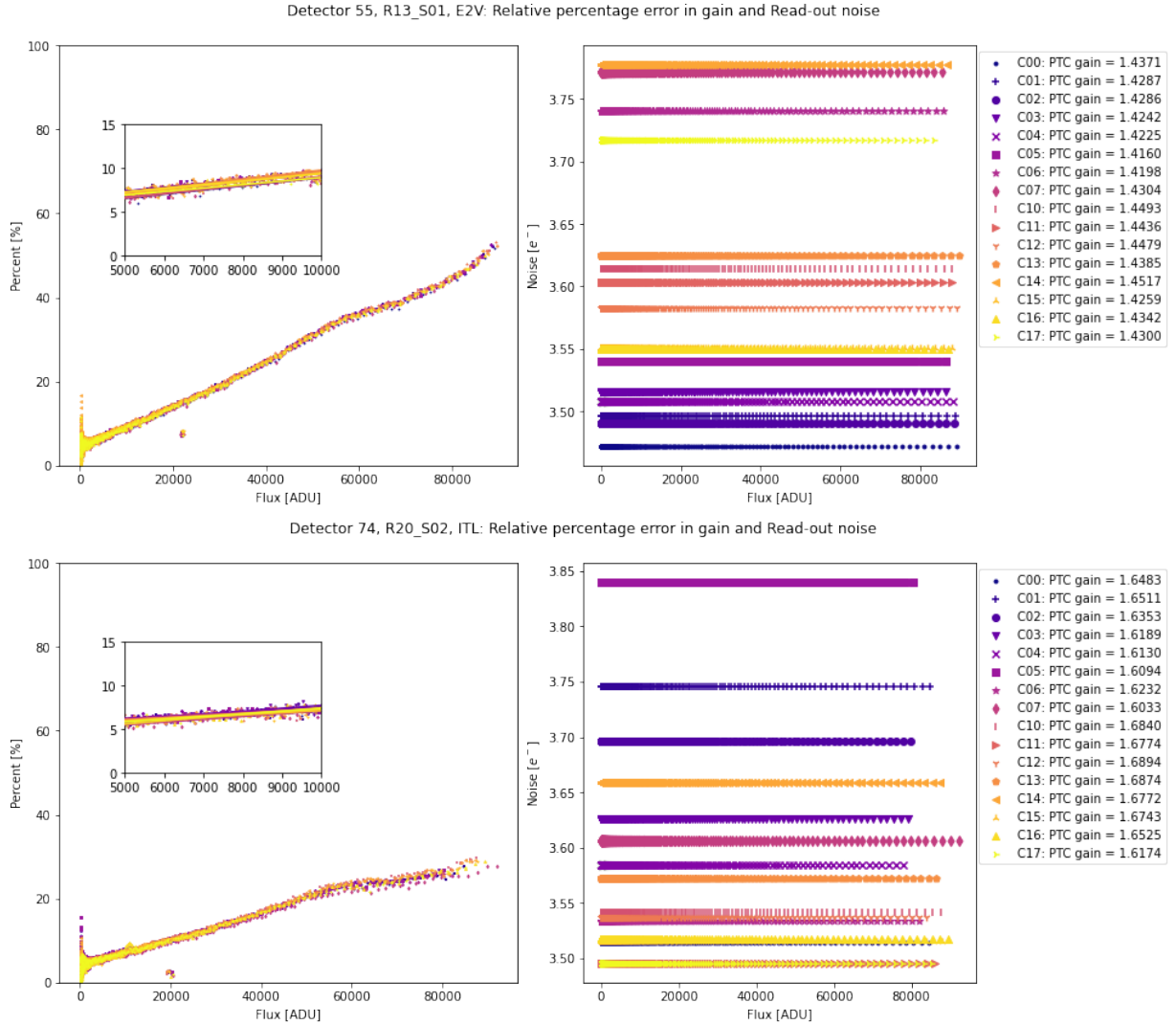


Figure 6: Relative percentage error between the gain estimated by the PTC and the gain calculated from two flat images (left), and the read-out noise of each amplifier (right), using the initial code. In the upper panel, it is shown for detector 55 (R13_S01), whose vendor is E2V, and in the lower panel for detector 74 (R20_S02) from the vendor ITL. Each color and symbol represents the relative percentage error for one of the 16 segments that make up each CCD. The embedded image in the left panels shows the percentage error between 5000 and 10000 ADU (low flux regime), in which a linear fit is made. The data used to construct these plots consider only those below the PTC turnoff.

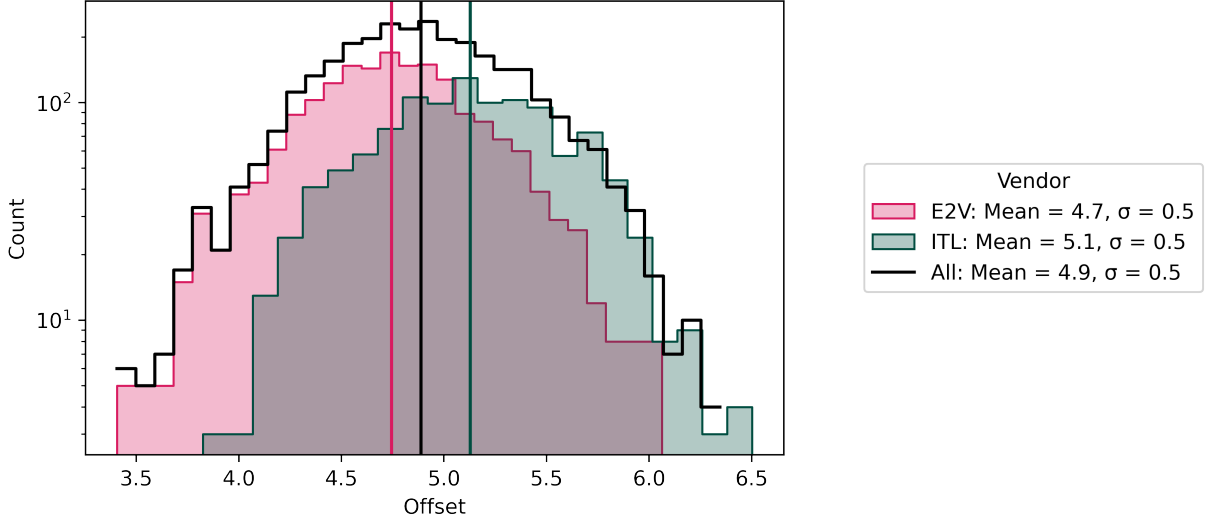


Figure 7: Histograms with the offset value obtained from the linear fit for flows between 5000 and 10000 ADU for the relative percentage error between gains. In magenta is shown the distribution for E2V, with a mean of (4.7 ± 0.5) %, and in blue for ITL, with a mean of (5.1 ± 0.5) %. The distribution in black represents the histogram of all data without discriminating by vendor, with a mean of (4.9 ± 0.5) %. The vertical lines represent the value of the mean for each of the distributions.

3.2.1 Simulation

The methodology described in section 3.2 and the use of the LSST software version *w_2022_27* led us to the results seen in Figures 6 and 7. Figure 6 shows the relative percent error between the gains over the flow range below the PTC turnoff for E2V sensor 55 (top panel) and ITL sensor 74 (bottom panel). The figure for each sensor has on the left an embedded plot showing the behavior between 5000 and 10000 ADU with its respective linear fit; on the right is the error of each of the CCD segments for the same flow range. We see in the embedded plot that the relative error has an offset higher than 5 % for these two sensors, so we made a histogram with the offset values for the entire focal plane and verified if this behavior is generalized. Figure 7 confirms that this relative error, on average, is a behavior exhibited by all sensors. We consider a base error of ~ 5 % to be relatively high, so we decided to investigate this problem through simulations.

Different variables could cause the problem described above to arise: an over-estimation of the readout noise, the mask used in the images is affecting, or another factor, such as the assumption that the distribution is Gaussian for the operation between the flat images given by

$$\frac{(I_1 - I_2)^2}{I_1 + I_2} \quad (8)$$

as it is being assumed in the *w_2022_27* version of the *DM stack*. If the distribution is not Gaussian, the distribution statistics are modified. We explored 3 cases through simulation to rule out or confirm variables, as described below:

- **Case 1 - Noise over-estimation:** Two data sets were constructed following a Poisson distribution for the flow, with an expected value between 5000 and 10000 ADU. In our case, we chose 5000 ADU. The distribution is then:

$$f(k; \lambda) = \frac{\lambda^k e^{-\lambda}}{k!} \implies f(k; 5000) = \frac{5000^k e^{-5000}}{k!} \quad (9)$$

where the expected value is λ , and k is the number of events. To the data following this distribution, we add a Gaussian noise whose mean is zero, and the value which gives the dispersion we will assume as the read-out noise, that is:

$$p(x) = \frac{1}{\sqrt{2\pi\sigma^2}} \exp\left(-\frac{(x-\mu)^2}{2\sigma^2}\right) \implies p(x) = \frac{1}{\sqrt{2\pi N^2}} \exp\left(-\frac{x^2}{2N^2}\right) \quad (10)$$

where the mean is μ , σ is the standard deviation, and N is the read-out noise, which we assume. Finally, we employ the methodology described in 3.2 for all types of gain correction: NONE, SIMPLE and FULL, and calculate the relative error using a base gain (we choose a value of 2.0) to verify if we can recreate what is observed in figure 6, i.e., a base error above 5 %.

- **Case 2 - Pixel masks:** As a next step, pixel masks are added to case 1. For this, the respective mask is extracted from each flat image, where each flat has an average of 5000 ADU counts. This mask filters out suspicious, bad, dead, and saturated pixels. A Poisson distribution is then generated with the dimensions of one of the CCD segments for which the masks were extracted, that is, $size_x = 2002$ and $size_y = 512$, with its respective Gaussian noise. The respective mask is applied to each array using the *Numpy* function (Harris et al., 2020) *ma.masked_where*.

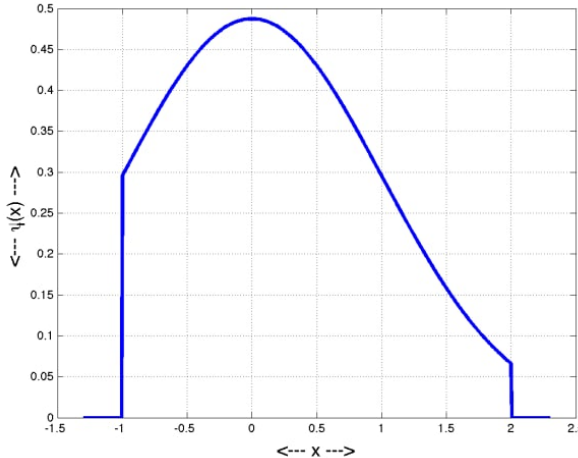


Figure 8: Truncated Gaussian distribution with both zero mean and standard deviation, $\psi(0, 1, a = -1, b = +2; x)$. Figure is taken from Burkardt (2014).

- **Case 3 - Statistics control:** To case 2, we add statistics control, i.e., we assume that the distribution of 8 is Gaussian, and we cut the distribution as it was done in the section 3.2, only in this case we keep all the data that are within 5.5σ of the mean, and we perform three iterations. Suppose the distribution of 8 is Gaussian. In that case, it must be satisfied that the mean of the truncated and original distribution is the same if symmetric cuts are made. When truncating non-symmetrically, the mean of this distribution is:

$$\mu = \bar{\mu} - \bar{\sigma} \frac{\phi(0, 1; \beta) - \phi(0, 1; \alpha)}{\Phi(0, 1; \beta) - \Phi(0, 1; \alpha)} ; \alpha = \frac{a - \bar{\mu}}{\bar{\sigma}}, \beta = \frac{b - \bar{\mu}}{\bar{\sigma}} \quad (11)$$

where α and β are standardized variables, a and b are the cutoff values for each side of the distribution, $\bar{\mu}$ and $\bar{\sigma}$ are the statistics of the original distribution, ϕ is the normal PDF, and Φ is the normal CDF. This case is illustrated in Figure 8 for $a = -1$ and $b = +2$. However, if $-a = b$, i.e., the distribution is symmetrically truncated, the numerator of the second term in the above equation becomes zero and is reduced to

$$\mu = \bar{\mu} \quad (12)$$

which implies that the mean of the truncated and the original distribution are equal. Therefore, we use this result to calculate the expected value of the equation 3 and thus find the gain solutions for the NONE, SIMPLE and FULL corrections. As an additional step, we check the shape of the distribution of 8; in case it is not Gaussian, no truncation is made to the distribution, and the expected value of the equation 3 is calculated with arithmetic mean.

3.3 No linearity Correction

To see the effect of linearity correction on the shape of the PTC and its parameters, we used a Spline linearizer with 12 nodes for detectors 32 (ITL) and 139 (E2V). This linearizer was generated by Jeronimo⁵ and in his analysis found that a Spline with 12 equally spaced nodes greatly corrects the effect of the nonlinearity and decreases the dispersion in the residuals. All configurations were the same, except, of course, the linearity correction (see table 1).

Table 1: Configuration used to generate the PTCs. The linearity correction is performed in this case, “doLinearize: true”.

Configuración			
doWrite: true	doLinearize: true	doFlat: false	doInterpolate: false
doOverscan: true	doCrosstalk: false	doFringe: false	doSaturation: false
doAssembleCcd: true	doBrighterFatter: false	doApplyGains: false	doSaturationInterpolation: false
doBias: true	doDark: true	doDefect: true	growSaturationFootprintSize: 0
doVariance: true	doStrayLight: false	doNaNMasking: true	ptcFitType: EXPAPPROXIMATION

Subsequently, plots of $\frac{Variance}{Mean}$ vs $Mean$ are constructed, so that the variance is normalized. Thus, it is analyzed whether the bump between 50000 and 60000 ADU is corrected. In addition, a relative percentage

⁵Jerónimo was my partner during this internship, who worked on the sister project Study of the Linearity of the CCDs of the Vera C. Rubin Observatory

error between the parameters obtained from the PTC fit with and without correction for linearity is calculated to quantify the effect on these. Finally, we checked whether the parameters and/or the shape of the PTC changed concerning its version without correction for nonlinearity.

3.4 Crosstalk Correction

The full focal plane readout of the LSSTCam can reach a readout time of 2s, so the combination of high speed, high resistivity silicon components, and close spacing between each channel makes the LSSTCam more susceptible than any other mosaic camera to electronic crosstalk (O'Connor, 2015).

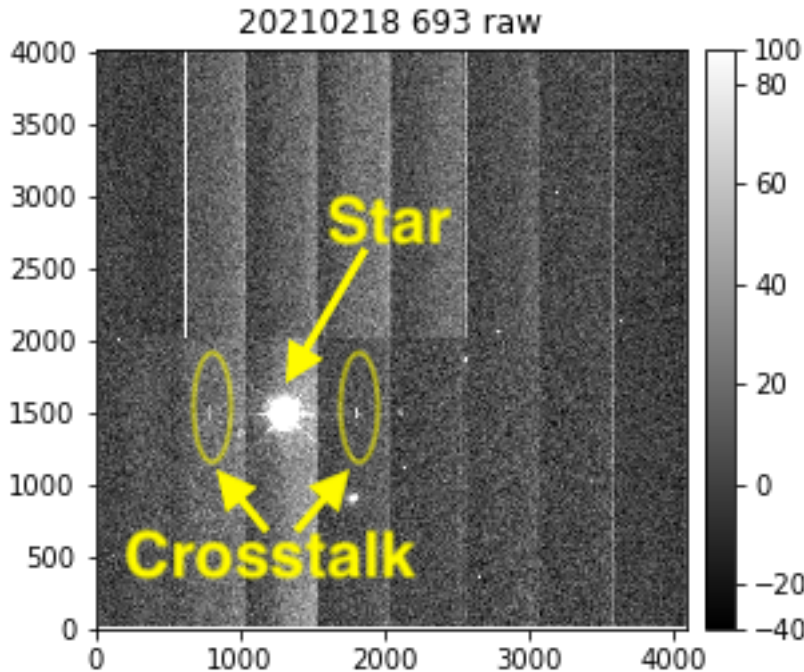


Figure 9: Image of a bright star taken with the 1.2m auxiliary telescope at the Vera Rubin Observatory. Segments adjacent to the bright start image show crosstalk.

Electronic crosstalk occurs in CCDs that contain several channels that are read simultaneously and coupled so that a channel that detects a bright source will cause a ghost image to be generated in adjacent segments due to this coupling (Snyder et al., 2020). This effect is presented in figure 9, where “ghost” signals are observed in the lateral segments of the detector. Figure 10 shows a heat map on the left for ITL detector 32 and on the right for ITL detector 139, where the highest crosstalk coefficients are in blue colors, and it is observed that the crosstalk pattern is different per vendor. These same coefficients are entered into a configuration file in the LSST software to re-generate the PTC with this correction.

Finally, as in the section 3.3, we checked whether the parameters and/or the shape of the PTC changed concerning its version without correction for crosstalk.

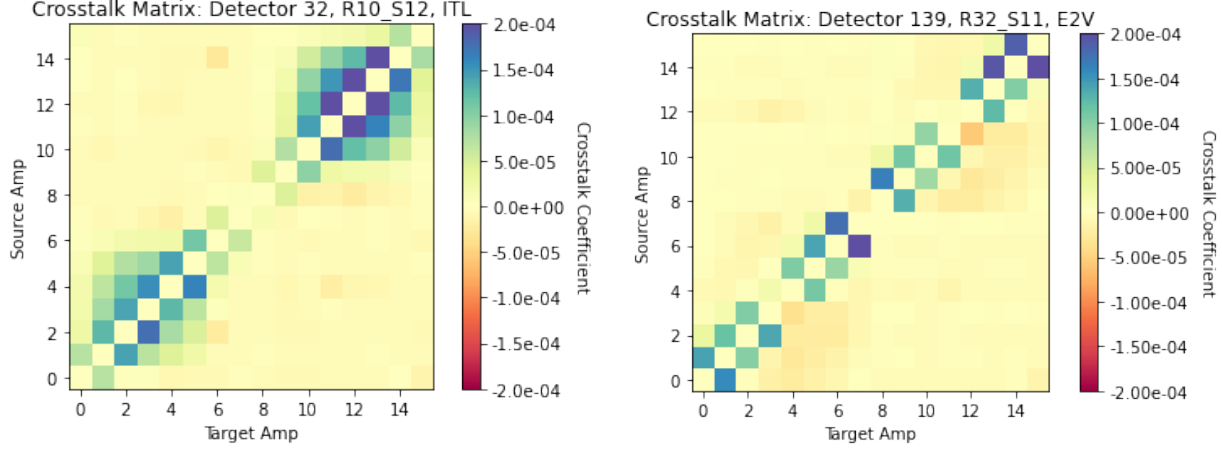


Figure 10: Crosstalk matrix on the left for detector 32 (ITL) and on the right for 139 (E2V).

4 Results

4.1 PTC

As part of this project, an initial and fundamental task was to use the PTC to determine the essential parameters of each CCD segment across the focal plane, using the *DM stack*. This has already been done by SLAC National Acceleration Laboratory⁶ (hereafter SLAC) for this very run (SLAC heat maps BOT 13144) and here we seek to reproduce their results.

Initially, we generated the PTCs by CCD for the entire focal plane, as shown in Figure 11, to detect PTCs with abnormal behavior and low PTC-turnoff (below 40000 ADU). Detectors found with low PTC-turnoff and/or misclassified are recorded in the table 2. In addition, a visual inspection showed that about 60 % of the detectors have at least one segment showing *Downing dip*.

Subsequently, we generate heat maps for the entire focal plane similar to those performed by SLAC, shown in the panels of Figure 12, for the parameters estimated by the fit to the PTC: gain and read noise in the upper left and right panel, respectively; a_{00} and turnoff in the lower left and right panel, respectively. A bimodality is found in the gain and a_{00} value (which accounts for the B-F effect); the more reddish values dominate in the E2V sensors, while the more yellow values dominate in ITL; this means that the E2V vendor's detectors have in general a lower gain, but a more negative B-F effect coefficient concerning ITL. Whereas, for readout noise and turnoff, no relevant effect is exhibited due to the vendor.

El comportamiento descrito anteriormente por los mapas de calor son reforzados por los histogramas de la figura 13, los cuales revelan la clara bimodalidad para la ganancia y a_{00} y un comportamiento más generalizado para el ruido de lectura y el turnoff. La ganancia tiene un valor promedio para los sensores de E2V de 1.49 ± 0.05 y de 1.69 ± 0.05 e^-/ADU para ITL. El coeficiente del B-F effect tiene un valor medio de $(-3.0 \pm 0.1) \times 10^{-6}$ y $(-1.7 \pm 0.2) \times 10^{-6}$ para E2V e ITL, respectivamente.

⁶El código utilizado por SLAC está disponible en SLAC code

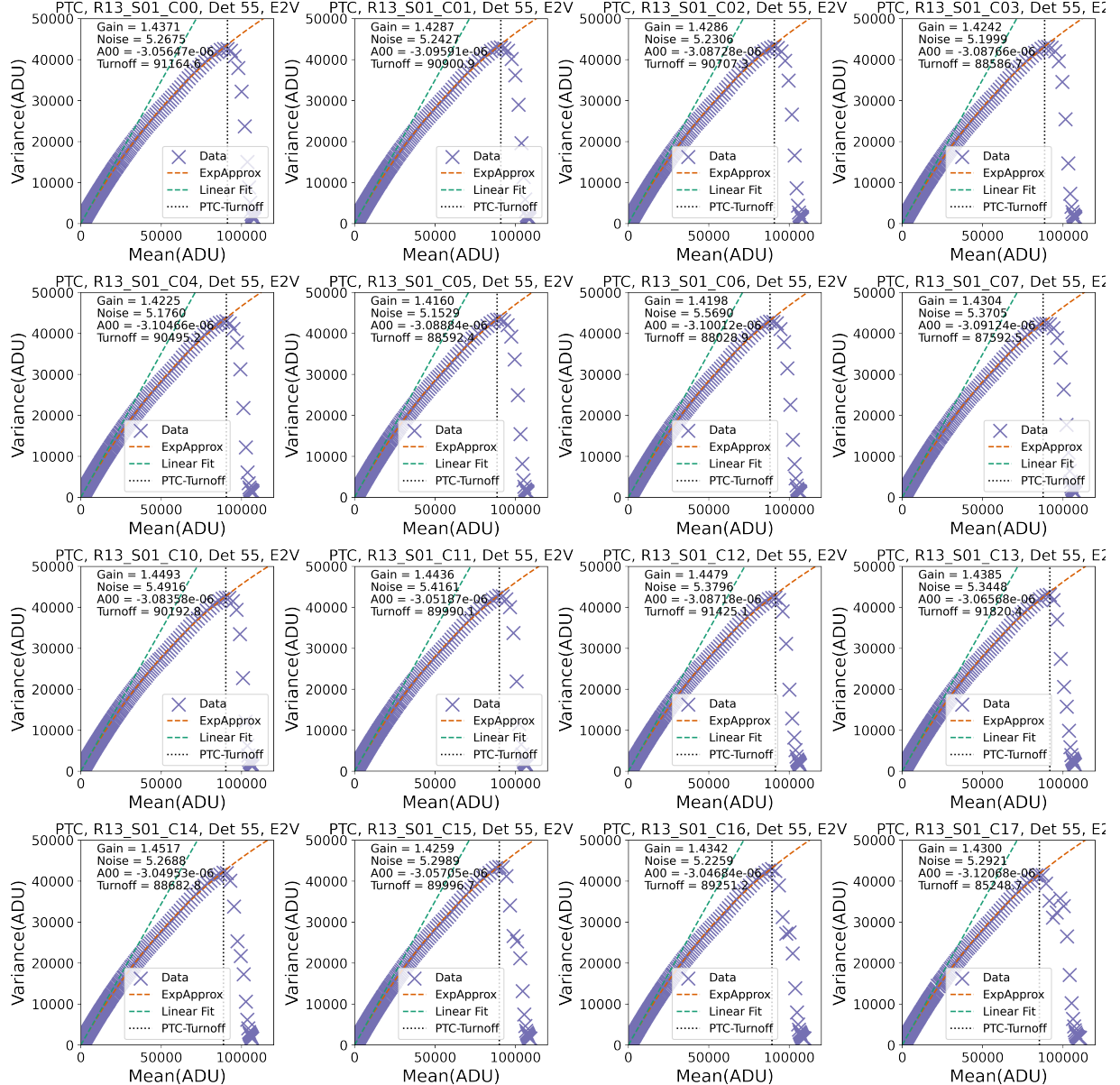


Figure 11: PTC for all segments of sensor 55 (E2V). Xs represent the data, the red line is the fit to the PTC by exponential approximation (eq. 1), and the green line is a linear fit. The parameters obtained from the fit to the PTC are the gain, the a_{00} parameter, the PTC turnoff (Max ADU), and the read noise.

Aunque en general los resultados entre este trabajo y SLAC son congruentes, encontramos diferencias en algunos segmentos para la ganancia, especialmente en el segmento C04 y C14 del detector 0 (R01_S00),

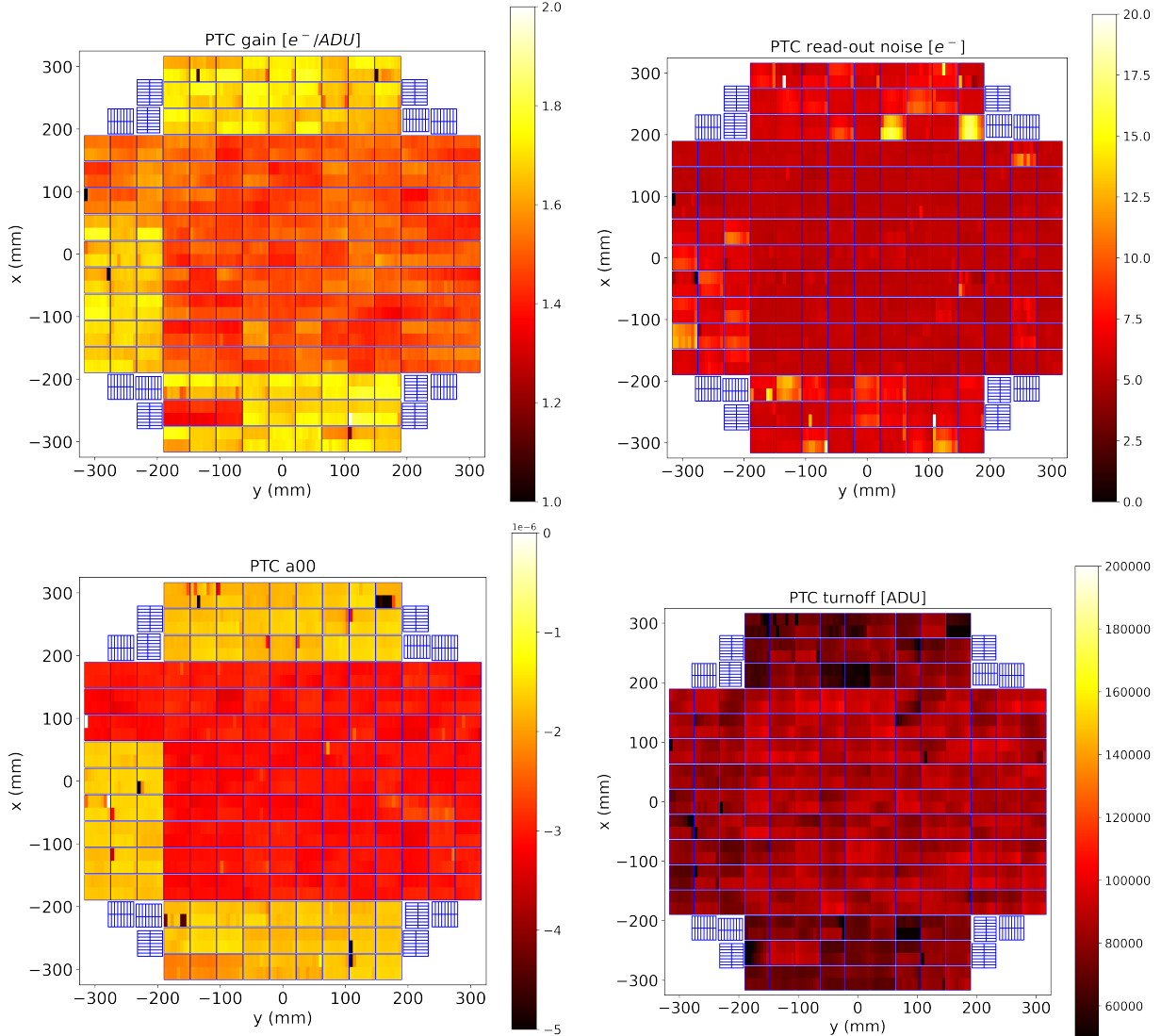


Figure 12: Heatmaps for the entire focal plane of the parameters obtained by the fit to the PTC in each segment that makes up the sensors. The upper panel shows the gain values on the left and the read noise on the right. The lower panel shows on the left the values of a_{00} , which are of the order of -1×10^{-6} , and on the right, the turnoff. These maps are a reproduction of those already constructed by SLAC for this same run 13144 (SLAC heat maps).

C00 del detector 22 (R03_S11) y C02 del detector 169 (R41_S21). Dos de estos segmentos se encuentran reportados en la tabla 2: para el segmento del detector 22 se reporta como muerto(?), mientras que para

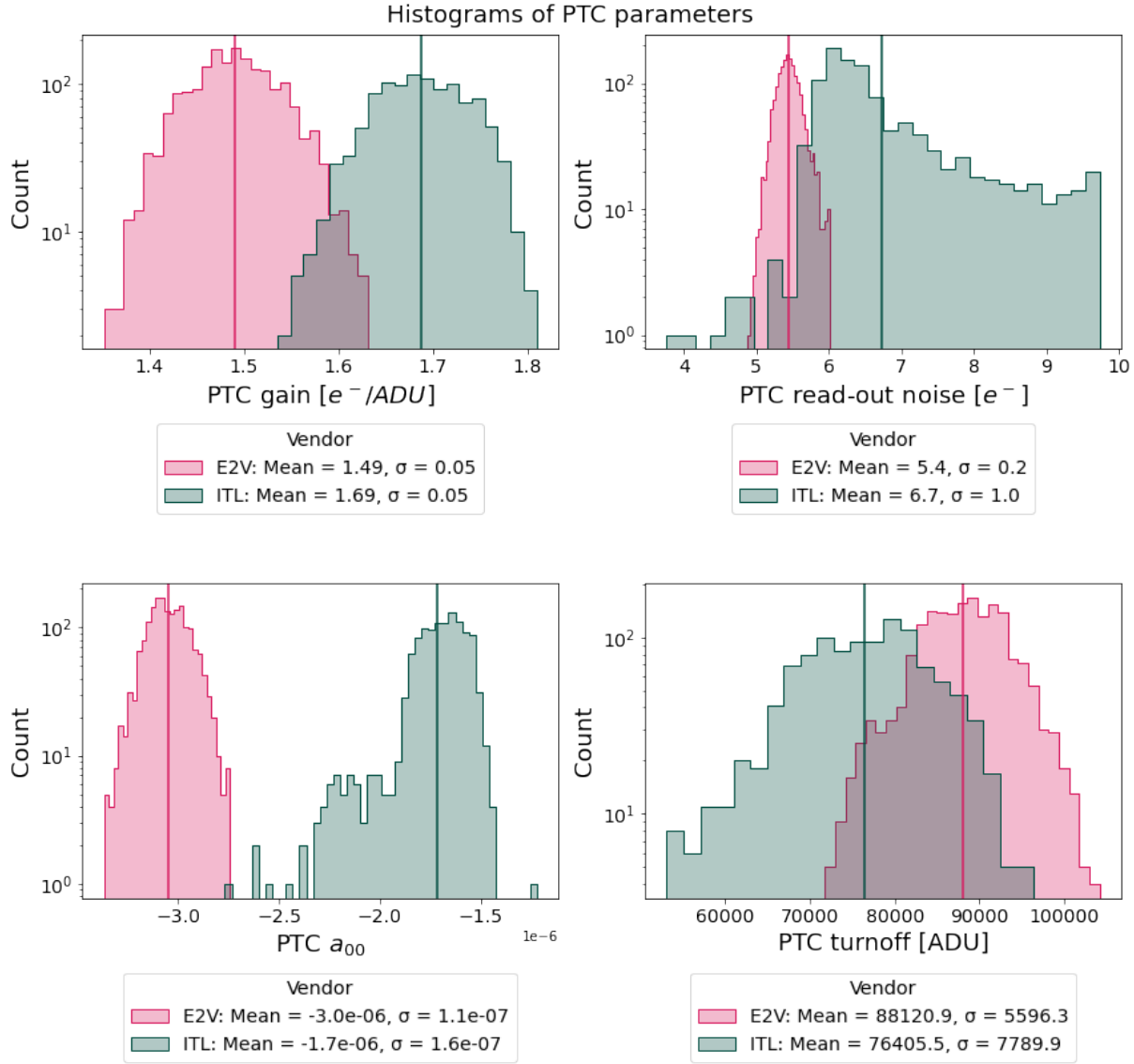


Figure 13: Histogramas para los parámetros obtenidos del ajuste a la PTC: la ganancia (arriba izquierda), ruido de lectura (arriba derecha), a_{00} (abajo izquierda) y turnoff (abajo derecha), cada una de las distribuciones se muestra por fabricante, en magenta para E2V y en azul para ITL. Las líneas verticales representan la media de cada distribución.

el segmento del detector 169 hay una mala clasificación por parte del algoritmo de la ubicación del PTC-turnoff. No obstante, estas fueron las diferencias más notorias que pudieron encontrarse visualmente, para determinar con exactitud las diferencias que existen hay efectuar un análisis más detallado con los respectivos códigos usados y sus versiones, pues aunque se usaron las mismas imágenes pueden existir diferencias entre los algoritmos que conduzcan a diferencia en los pixeles usados para el cálculo debido a las máscaras utilizadas, diferencias en la reducción de las imágenes (Instrument Signature Removal o ISR), diferente rechazo de outliers, entre otras.

```

206      # Cannot assume that the mean values are sorted
207      ptc_turnoff = max(mean[index])

(a) Código de eotest

839      # Discard points when the variance starts to decrease after two
840      # consecutive signal levels
841      goodPoints = self._getInitialGoodPoints(meanVecOriginal, varVecOriginal,
842                                              self.config.minVarPivotSearch,
843                                              self.config.consecutivePointsVarDecreases)
844

857      # Save the point where the variance starts decreasing as the
858      # PTC turnoff point
859      ptcTurnoff = meanVecOriginal[goodPoints][-1]
860      dataset.ptcTurnoff[ampName] = ptcTurnoff

(b) Código de DM stack

```

Figure 14: Códigos utilizados para calcular el PTC-turnoff en eotest (a), empleado por SLAC, y DM stack (b), código oficial para los datos del LSST.

Por otro lado, aunque para el PTC turn-off en general se observa un comportamiento similar para los sensores entre este trabajo y SLAC, la forma de determinación empleó métodos diferentes, tal y como se evidencia en la figura 14, donde *eotest* define el PTC-turnoff como el punto donde la varianza es máxima, teniendo en cuenta que este valor máximo se determina entre los datos cuyos residuales se encuentren por debajo de 5σ ; mientras que *DM stack* define a este como el punto en el que la varianza comienza a decrecer monotónicamente por al menos dos puntos (el número de puntos que debe decrecer se puede modificar en la función *_getInitialGoodPoints*). Por parte de SLAC el FWC encontrado fue de ~ 90000 e⁻ *referencia?*, mientras que en este trabajo encontramos un valor un valor promedio de turnoff con un valor de 83240 ADU, cuya equivalencia en electrones sería un valor aproximado del FWC de 130000 ± 10000 e⁻.

Table 2: Detectors containing segments with low PTC-turnoff (below 40000 ADU), PTC-turnoff misclassified by the algorithm, bad segments, or differences observed concerning the results obtained by SLAC (parameters in red). Presented for each segment is the detector ID (col1), detector number (col2), vendor (col3), affected segment (col4), PTC parameters (gain, B-F effect, and turnoff coefficient; cols 5, 6, 7, and 8, respectively), detected problem (col9).

Detector ID	Det Num	Vendor	Amp	Gain [e^-/ADU]	Read Noise [e^-]	A_{00}	Turnoff [ADU]	Issue
R01_S00	0	ITL	C04	1.5833	6.2061	-2.0160 $\times 10^{-6}$	73461.2	SLAC diff
R01_S00	0	ITL	C14	1.7514	6.4150	-2.1907 $\times 10^{-6}$	68032.3	SLAC diff
R01_S20	6	ITL	C00	1.5354	11.1174	-4.1734 $\times 10^{-6}$	65371.7	SLAC diff
R01_S20	6	ITL	C05	1.4837	15.5104	-4.5175 $\times 10^{-6}$	76106.5	SLAC diff
R01_S20	6	ITL	C06	1.5104	13.5644	-4.3955 $\times 10^{-6}$	72293.9	SLAC diff
R02_S20	15	ITL	C17	1.67191	5.81973	-2.20396 $\times 10^{-6}$	30567.4	low PTC-turnoff
R03_S11	22	ITL	C00	15.2117	44.0087	-0.708105	223.072	SLAC diff - dead?
R10_S11	31	ITL	C10	1.63413	4.13177	-3.65785 $\times 10^{-6}$	32842.4	low PTC-turnoff
R20_S00	72	ITL	C17	0	0	nan	0	SLAC diff and dead
R20_S01	73	ITL	C00	1.6083	6.45279	-3.12539 $\times 10^{-6}$	35507.4	low PTC-turnoff
R20_S12	77	ITL	C00	1.59232	4.70427	-8.02249 $\times 10^{-6}$	26827.1	low PTC-turnoff
R30_S00	117	E'2V	C10	0	0	nan	0	SLAC diff and dead
R41_S20	168	ITL	C16	1.61074	6.07818	-1.98753 $\times 10^{-6}$	37863.2	low PTC-turnoff
R41_S20	168	ITL	C17	1.59228	9.57256	-2.54637 $\times 10^{-6}$	26120	low PTC-turnoff
R41_S21	169	ITL	C02	1.08095	62.8775	-4.52943 $\times 10^{-6}$	16237.9	SLAC diff and PTC-turnoff mismatch
R41_S21	169	ITL	C11	1.61255	5.23312	-2.61051 $\times 10^{-6}$	32467.3	PTC-turnoff mismatch
R41_S21	169	ITL	C15	1.59804	5.21757	-2.31531 $\times 10^{-6}$	39151.3	PTC-turnoff mismatch
R41_S22	170	ITL	C10	1.60171	4.76741	-3.2105 $\times 10^{-6}$	32369.9	low PTC-turnoff
R42_S00	171	ITL	C17	1.65116	6.4254	-3.09362 $\times 10^{-6}$	30253.3	low PTC-turnoff
R43_S10	183	ITL	C17	1.59721	8.53352	-2.46596 $\times 10^{-6}$	30195.2	low PTC-turnoff
R43_S22	188	ITL	C00	1.6348	5.28826	-4.64678 $\times 10^{-6}$	21477.5	SLAC diff
R43_S22	188	ITL	C01	1.6348	5.28826	-4.64678 $\times 10^{-6}$	21477.5	low PTC-turnoff
R43_S22	188	ITL	C02	1.55382	6.94625	-7.40255 $\times 10^{-6}$	30764.3	low PTC-turnoff
R43_S22	188	ITL	C03	1.56826	7.24918	-4.92713 $\times 10^{-6}$	38222.4	low PTC-turnoff
R43_S22	188	ITL	C04	1.58147	3.76291	-4.88158 $\times 10^{-6}$	38143.6	low PTC-turnoff

4.2 Gain from flat pairs

La ganancia de cada uno de los segmentos de la cámara es obtenida inicialmente mediante la PTC. Sin embargo, este método requiere mayor tiempo para ser generado dado que es un ajuste sobre un gran rango en flujo. Por ello se tiene un método alternativo, que llamaremos *Ganancia por pares de flat*, que es menos costoso en tiempo. En la figura 15 se observa los valores de ganancia para flujos desde 0 a ~ 120000 ADU en la izquierda, que incluye valores que han superado el umbral de saturación, dado por la línea vertical que marca el turnoff de la PTC para cada segmento, en este caso del detector 55; a la derecha se muestran valores solo un poco más alejados del nivel de saturación (nosotros solo usamos datos por debajo del PTC-turnoff para el análisis de la ganancia por pares de flats) y en este rango se logra observar que hay un bache alrededor de los 60000 ADU, que es debido a la no linealidad, que se discutirá en la sección 4.3. En esta sección describimos las diferencias que encontramos entre la ganancia por PTC y la obtenida por pares de flats, una posible forma para disminuirlas y finalmente qué esperar de este segundo método respecto al primero.

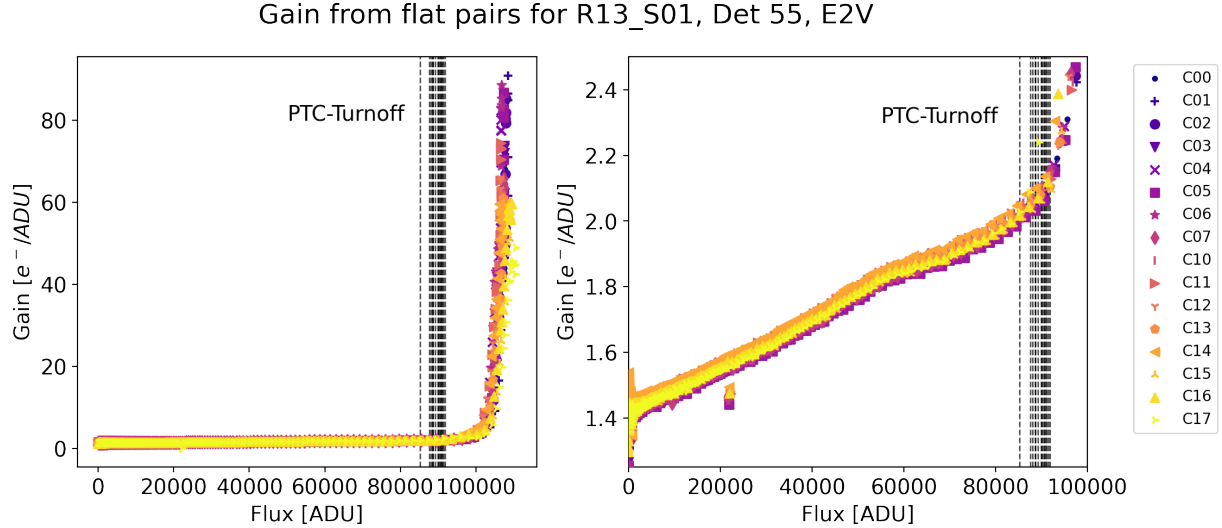


Figure 15: Valores de ganancia obtenidos por pares de flat para flujos hasta aproximadamente 120000 ADU para el detector 55 (R13_S01). En ambos paneles las líneas verticales discontinuas representan el valor del PTC turnoff para cada uno de los 16 segmentos del detector y las figuras de colores representan los valores de ganancia y flujo para cada segmento. El panel de la derecha muestra solo la región hasta el PTC-turnoff del panel de la izquierda.

Como también se mencionó en la introducción a la metodología, se utilizaron dos versiones de código (w_2022_27 y w_2022_32), donde la principal diferencia que a nosotros nos interesa es la que muestra la figura 16, que se da en la forma en la que se manejan los estadísticos para finalmente calcular la ganancia por pares de flats, donde w_2022_27 utilizaba la versión en rojo, que supone una distribución Gaussiana y trunca la distribución para rechazar outliers, y w_2022_32 utiliza la versión en verde, y es resultado de lo que nosotros analizamos y describiremos en breve: la distribución de la operación entre dos imágenes flats que conducen a calcular la ganancia no tiene una distribución Gaussiana, por lo que realizar un

truncamiento en la distribución altera el valor esperado para la ganancia.

```

@@ -758,7 +758,7 @@ def getGainFromFlatPair(self, im1Area, im2Area, imStatsCtrl, mu1, mu2,
758     758
759     759         ratioIm /= sumIm
760     760
761     -     const = afwMath.makeStatistics(ratioIm, afwMath.MEANCLIP, imStatsCtrl).getValue()
761 + + const = afwMath.makeStatistics(ratioIm, afwMath.MEAN, imStatsCtrl).getValue()
762     762         gain = 1. / const
763     763
764     764     if correctionType == 'SIMPLE':

```

Figure 16: Diferencia entre el código inicial y el código actual para el cálculo de la ganancia a partir de un par de flat fields.

La versión *w_2022_27* nos arrojó el resultado que se muestra en la figura 6, un error relativo porcentual entre la ganancia por PTC y por pares de flat a un flujo de 5000 ADU por encima del 5%, esto tanto para un detector de E2V (panel superior) como para uno de ITL (panel inferior). Este porcentaje tan alto a este flujo no era esperado, por lo que para indagar qué estaba generando este valor realizamos simulaciones, con la metodología descrita en la sección 3.2.1.

4.2.1 Simulation

A partir del resultado anterior, un error relativo entre las ganancias del 5 % a 5000 ADU, teníamos dos hipótesis: primero, las máscaras en las imágenes flat podrían estar afectando de alguna manera, si las máscaras de cada imagen eran muy diferentes y no se utilizaba la misma máscara para hacer los cálculos podrían generar este error relativo tan alto; segundo, si no son las máscaras qué en la estadística me está ocasionando este error.

Encontramos a partir de las simulaciones de la imagen flat de un segmento de CCD, utilizando una máscara de un segmento real, que utilizar una máscara para los dos flats, la unión de ambas máscaras o máscaras diferentes para cada uno, no daba cuenta del error del 5% a 5000 ADU, tal y como lo muestra el panel superior de la figura 17, lo único que podemos ver en este caso es que a mayor ruido de lectura, y al utilizar una corrección de tipo NONE, mayores son las discrepancias entre la ganancia esperada ($2 e^-/\text{ADU}$) y la calculada, pero las subsecuentes correcciones (SIMPLE y FULL) que sí tienen en cuenta el valor del ruido de lectura logran calcular de forma precisa el valor esperado de ganancia. No obstante, el panel inferior de esta figura, que incluye además de las máscaras estadísticos de control, me da cuenta en todos los casos de un error relativo porcentual entre la ganancia por PTC y pares de flats por encima del 5 %. En la siguiente sección (4.2.2) comprobamos esto con los datos reales.

4.2.2 Real data

En vista de los resultados obtenidos a partir de la simulación, se verificó si los resultados se mantienen con los datos reales y en efecto lo hacen. Hicimos esta comprobación en el detector 55 (R13_S01) para todos sus segmentos, como se muestra en las figuras 18 y 19, donde las cruces negras representan el valor de ganancia obtenida a partir de la PTC. La primera figura nuevamente revela que el uso de las máscaras (misma máscara utilizada para los cálculos, que es la unión de las máscaras individuales) y sin estadísticos

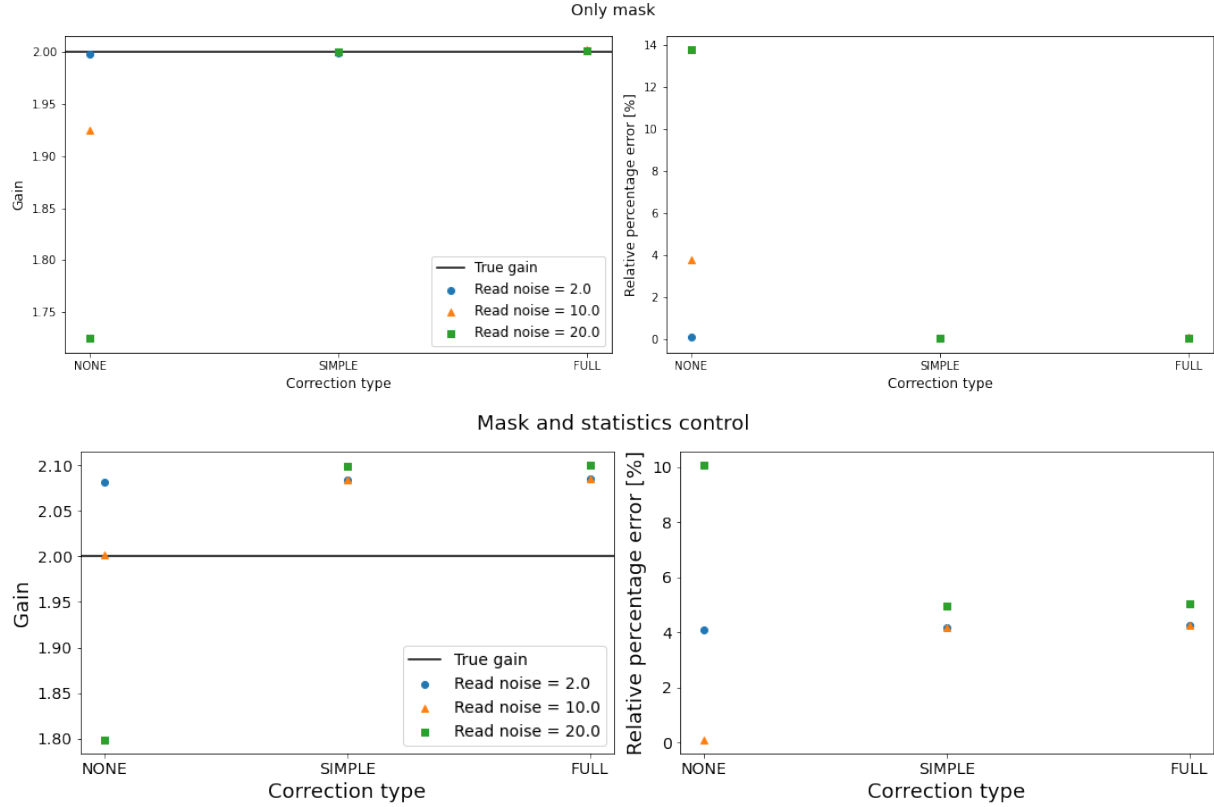


Figure 17: Resultados de la simulación para obtener la ganancia por pares de flats, en el panel superior utilizando únicamente máscaras y en el inferior añadiendo además estadísticos de control. El valor promedio de flujo de estos flats simulados es de ~ 5000 . Los paneles de la izquierda muestran el valor de la ganancia para 3 diferentes modelos y a la derecha el error relativo porcentual respecto al valor esperado de ganancia, $2 e^-/\text{ADU}$. En los paneles izquierdos la línea negra horizontal representa el valor de ganancia esperado y las figuras representan los diferentes valores considerados para el ruido de lectura: círculo azul de $2 e^-/$, triángulo naranja de $10 e^-/$ y cuadrado verde de $20e^-/$. Considerando estos ruidos de lectura se calculó la ganancia para tres modelos diferentes: NONE, SIMPLE y FULL.

de control no da cuenta de un error relativo mayor al 5 % para ningún segmento del detector, el máximo valor alcanzado es de 2.25 % a un flujo promedio de 5450 ADU. La segunda figura, que incorpora además los estadísticos de control, en cambio muestra que, en efecto, el manejo de los estadísticos está produciendo altas discrepancias entre la ganancia por PTC y la ganancia calculada por pares de flats llegando a alcanzar diferencias hasta del 9 % en uno de los segmentos a un flujo de 5450 ADU.

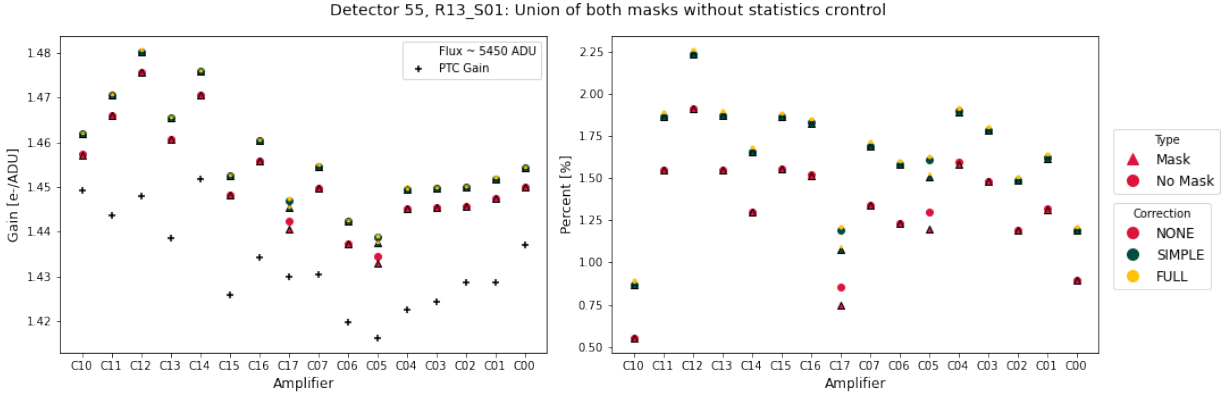


Figure 18: Valor de ganancia (panel izquierdo) y error relativo porcentual (panel derecho) para los 16 segmentos (amplifier) del detector 55 (R13_S01). En el panel izquierdo las cruces negras representan el valor de la ganancia por PTC. Para ambos paneles las figuras representan si el cálculo de la ganancia por pares de flats utilizó máscara (triángulos) o si no la utilizó (círculos), y los colores están asociados al modelo empleado para determinar la ganancia: NONE, SIMPLE y FULL. Para la máscara se utilizó la unión de las máscaras de ambas imágenes flat por segmento y no se utilizó estadísticos de control.

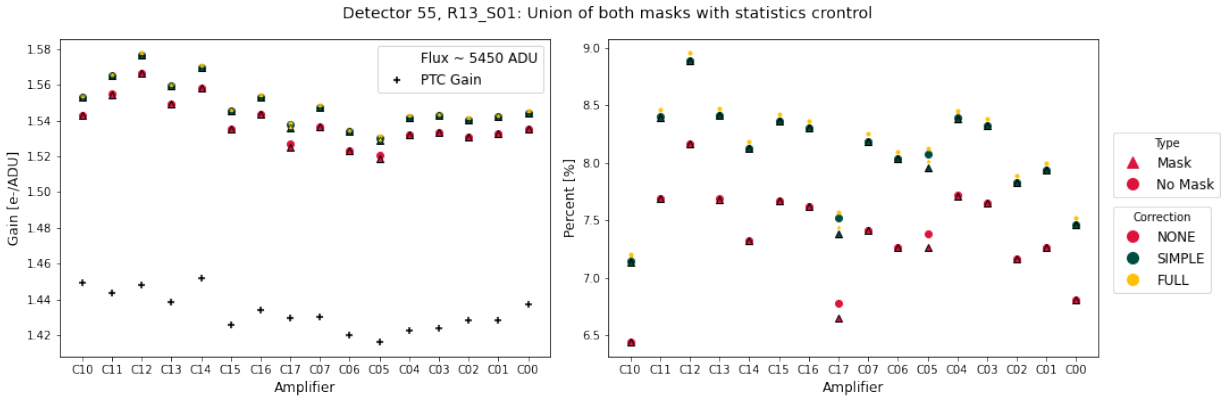


Figure 19: Ver descripción de la figura 18. En esta figura sí se empleó estadísticos de control.

Posteriormente, realizamos gráficas de las distribuciones para la operación entre las imágenes flats dadas por la ecuación 8, la cual es el argumento de la ecuación de Lupton (ec. 3) y está directamente relacionado con la ganancia. Los resultados que obtuvimos se muestran en la figura 20 para cada segmento del detector y revelan que la forma de esta distribución dista de ser Gaussiana, por lo que efectuar truncamientos a esta distribución produce un cambio en el valor de la media, que ya no coincide con la media de la distribución original, y por tanto dando un valor diferente de ganancia al esperado.

Finalmente, sin efectuar truncamiento en la distribución, como lo muestra el código en verde de la figura 16, construimos nuevamente las figuras de error relativo porcentual para la ganancia y obtuvimos

el resultado de la figura 21 que revela en su imagen embebida que para un flujo de 5000 ADU que la diferencia entre ambas ganancias ahora está por debajo del 5 % como lo indicaban las simulaciones. Con este resultado estimamos una relación general para la ganancia teniendo en cuenta las distribuciones para los parámetros del ajuste lineal, como se muestran en la figura 22, que fue efectuado entre los 5000 y 10000 ADU. En esta figura se observa a la izquierda arriba la distribución de las pendientes por fabricante que revela una clara bimodalidad, teniendo una pendiente ligeramente mayor los detectores de E2V respecto a ITL, con una media de (0.00046 ± 0.00004) y (0.00027 ± 0.00004) %/ADU, respectivamente. En el panel inferior de esta figura tenemos el intercepto con el eje y (es decir, con el eje del porcentaje de error entre las ganancias) y muestra que hay una media global en los detectores, sin distinción apreciable por fabricante, con un valor de (-0.5 ± 0.5) %. Así las cosas, por fabricante, el error relativo porcentual entre los 5000 y 1000 ADU está dado por

- E2V: $Error_{2Gain} = (0.00046 \pm 0.00004)F - (0.5 \pm 0.5)$, donde el intervalo de error es de $(1.8 \pm 0.7, 4.1 \pm 0.9)$ %.
- ITL: $Error_{2Gain} = (0.00027 \pm 0.00004)F - (0.5 \pm 0.5)$, donde el intervalo de error es de $(0.85 \pm 0.7, 2.2 \pm 0.9)$ %.

4.3 Crosstalk and Linearizer

Parte de los análisis finales que efectuamos durante esta pasantía consistió en cuantificar y decidir si el efecto de crosstalk y la no linealidad tienen impacto en la forma de la PTC y/o de los parámetros fundamentales: ganancia, ruido de lectura, coeficiente del B-F effect y turnoff.

Como se describió en la sección 3.4, tuvimos acceso a las matrices de crosstalk para el detector 32 (ITL) y el 139 (E2V), que se muestran en la figura 10. Como resultado de la metodología de dicha sección obtuvimos que las diferencias de la PTC corregida y no corregida por crosstalk es muy baja, como se muestra en las figura 23 y 24, donde se muestra que considerando la región por debajo de saturación, la diferencia entre las varianzas está por debajo siempre de 0.1 ADU, mientras que en los parámetros la mayor variación es de $\sim 0.1\%$ en el ruido de lectura y en el coeficiente del B-F effect y $\sim 0.07\%$ en la ganancia y el turnoff. Las mayores diferencias se encontraron en los segmentos del detector de ITL. De acuerdo con lo anterior, llegamos a la conclusión de que el crosstalk no tiene un efecto importante y no es necesario corregir por este efecto ya que la diferencia en los parámetros es pequeña y no altera la forma de la PTC.

Finalmente, se aplicó el linealizador spline cúbico de 12 nodos para verificar su impacto en la forma de la PTC. Se presenta en la figura 25 el resultado de corregir solo por crosstalk (puntos naranja), solo por la no linealidad (diamantes azules), corregidos por ambos efectos (triángulos grises) y los datos sin corregir (cuadrados magenta). Vemos que los datos sin corregir presentan un bache alrededor de los 60000 ADU, mientras que los datos corregidos por crosstalk se ubican siempre en la misma posición de los datos no corregidos (por tanto también muestran el bache), los datos corregidos por la no linealidad lo aplanan. De acuerdo con lo anterior, hacer las dos correcciones a los datos no tiene mayor efecto al que se obtiene corrigiendo solamente por la no linealidad. Nuevamente comprobamos que el crosstalk no es una corrección necesaria dado que no afecta ni la forma, ni los parámetros de la PTC.

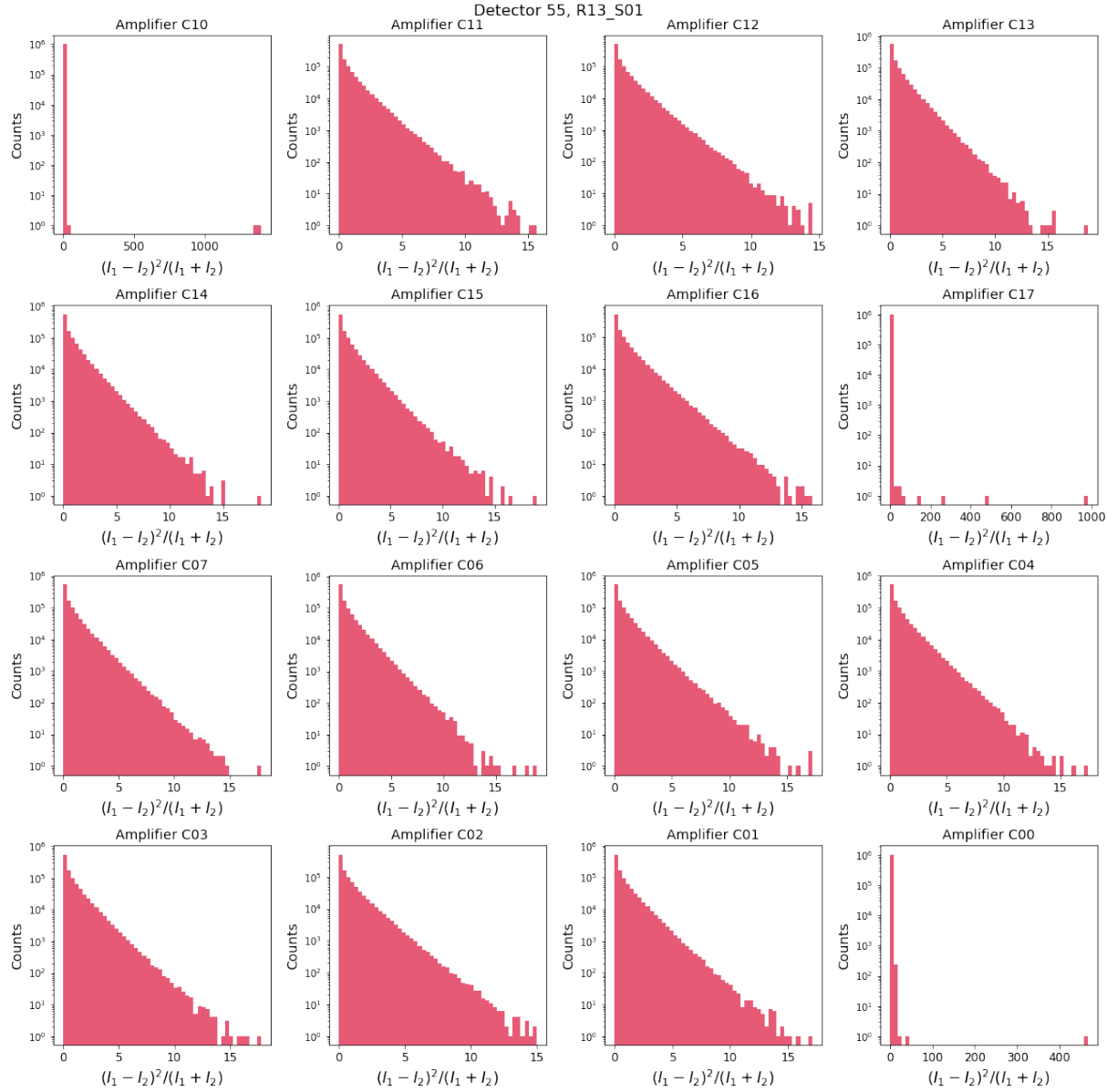


Figure 20: Histograma de la distribución para $\frac{(I_1 - I_2)^2}{I_1 + I_2}$ para cada segmento del detector 55 (R13_S01).

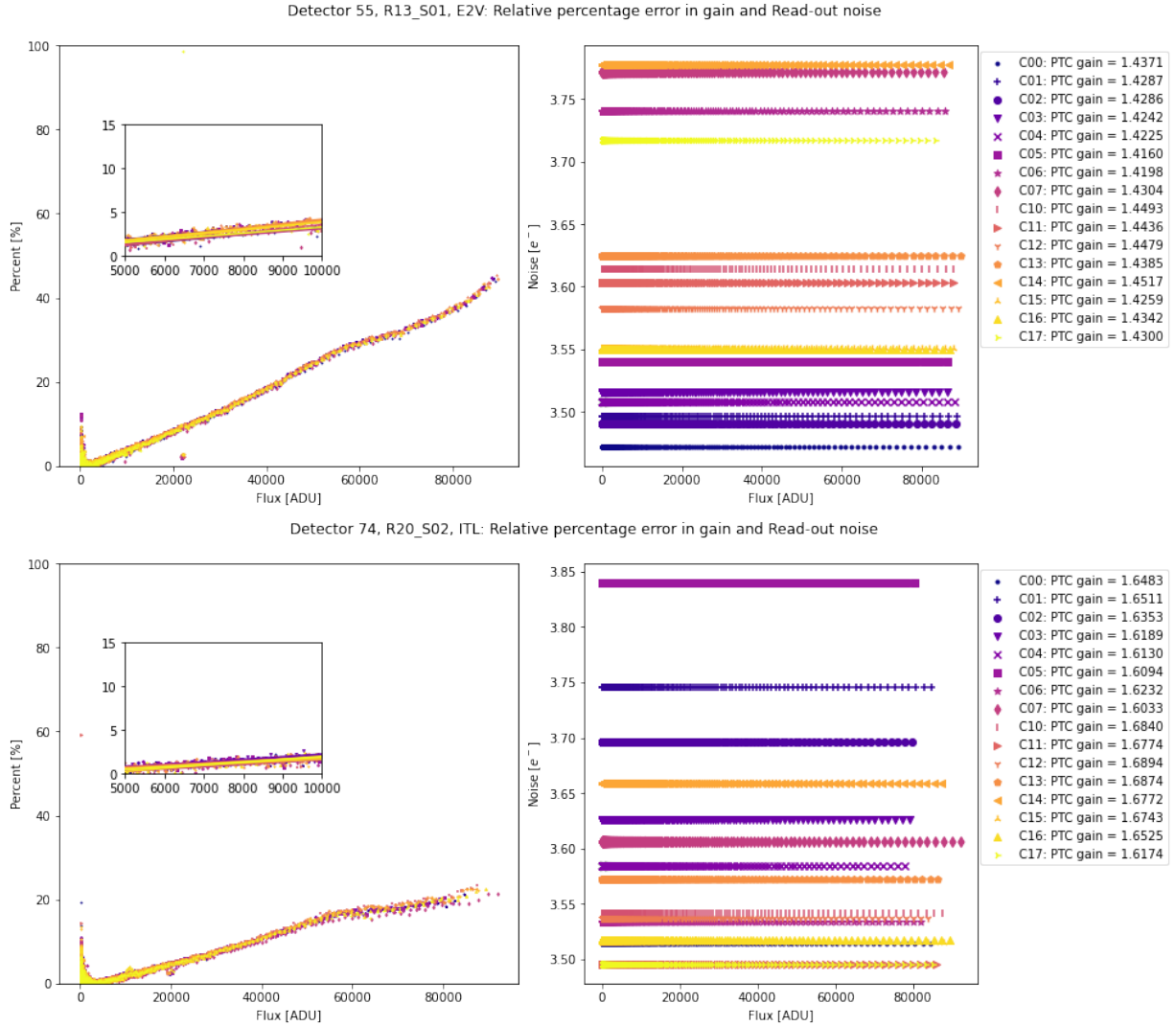


Figure 21: Refer to the description of the figure 6. This plot uses the updated code that does not use clipped mean.

5 Conclusions

We present in this report a list of the sensors that present differences in the parameters with those obtained by SLAC, a PTC with low turnoff, and an inadequate classification of the same so that they can be reviewed later. We use the default value to determine the turnoff via *DM stack*: decrease by at least 2 points to indicate shutdown.

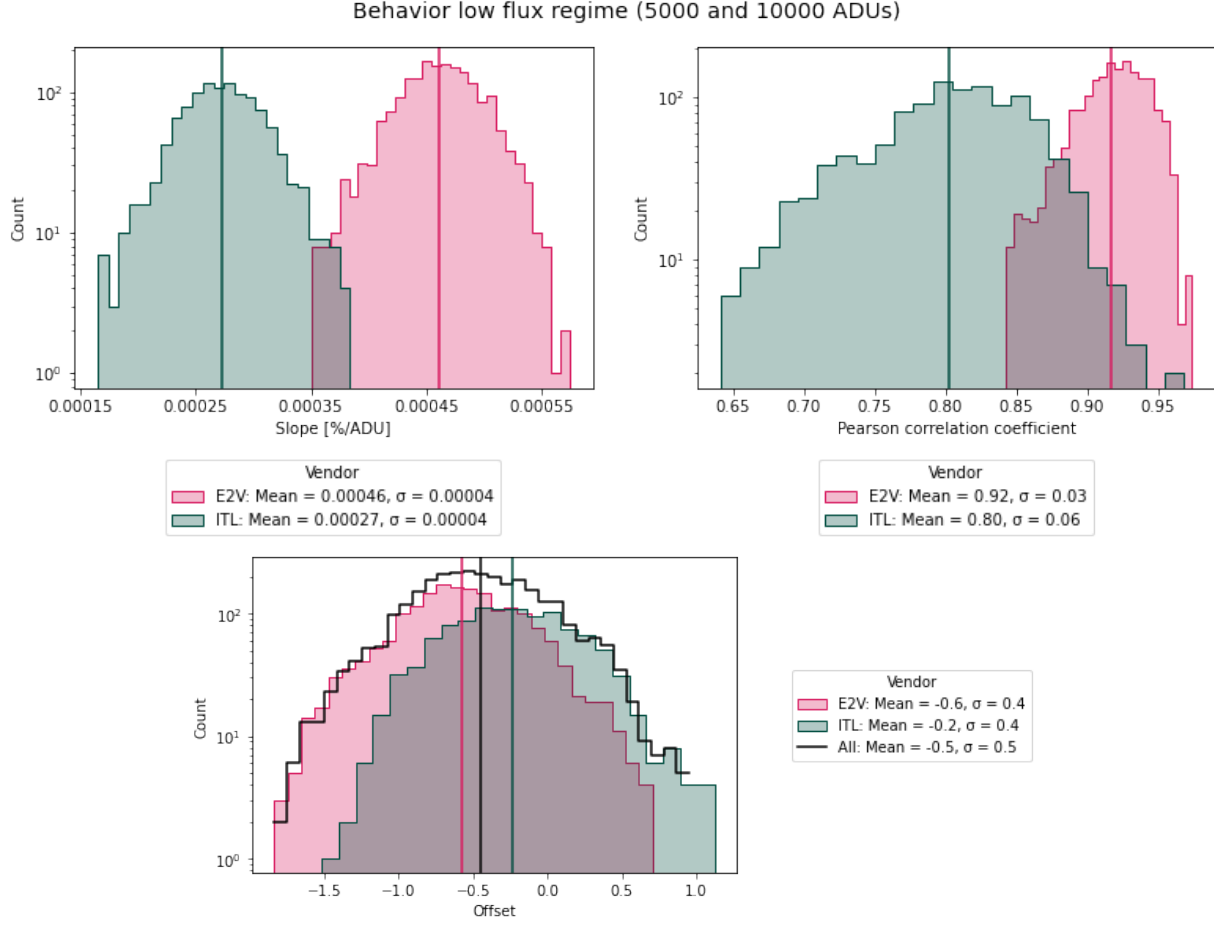


Figure 22: Histogramas para la pendiente (arriba izquierda), el coeficiente de correlación de Pearson (arriba a la derecha) y para el intercepto con el eje y (offset, panel inferior) que corresponde al ajuste lineal efectuado en la región de flujo entre 5000 y 10000 ADU para la ganancia. Para su construcción se utilizó el nuevo código y los colores representan el fabricante, E2V en rojo e ITL en azul. Las líneas verticales representan la media para cada caso.

We find in the PTC study that there is a bimodality per vendor for gain and a_{00} and a more generalized behavior for read noise and turnoff. The average value we found for the gain in the E2V sensors of 1.49 ± 0.05 and $1.69 \pm 0.05 e^-/\text{ADU}$ for ITL. The coefficient of the BF effect has an average value of $(-3.0 \pm 0.1) \times 10^{-6}$ and $(-1.7 \pm 0.2) \times 10^{-6}$ for E2V and ITL, respectively. In addition, ITL detectors present a higher read noise dispersion compared to E2V ($6.7 \pm 1.0 e^-$ and $5.4 \pm 0.2 e^-$, respectively). The results obtained in this work are generally congruent with those obtained by SLAC. However, the main difference was observed in the Full Well Capacity value: in this work, we found a value of $130000 \pm 10000 e^-$, while SLAC a value of $90000 e^-$, which is a product of the different ways of calculating the turnoff between *eotest* and *DM stack*.

The analysis between the gain obtained from a pair of flats and the gain obtained from the PTC initially yielded a relative percentage error for low fluxes (5K and 10K ADU) higher than 5%. This result led to a thorough investigation of its origin, finding that the distribution following the Lupton equation for flat images is not of Gaussian type, so the truncation of the distribution to calculate the statistics generating a shift of the mean value, and consequently, larger values of gain concerning the PTC gain. Therefore, this calculation was performed without truncation and obtained percentage differences between these two gains of $(1.8 \pm 0.7, 4.1 \pm 0.9)$ for E2V and $(0.85 \pm 0.7, 2.2 \pm 0.9)$ for ITL, where these intervals correspond to a flow region between 5000 and 10000 ADU. Consequently, the respective report was made and finally implemented in the main code.

Finally, the linearity correction fixes the observed bump around 50K-60K ADU. Whereas performing a correction for crosstalk does not affect the shape of the PTC, nor does it significantly modify the parameters. Therefore, we recommend correcting for linearity only.

References

- Astier, P., Antilogus, P., Juramy, C., Le Breton, R., Le Guillou, L., & Sepulveda, E. (2019). The shape of the photon transfer curve of ccd sensors. *Astronomy & Astrophysics*, 629, A36.
- Astropy Collaboration, Price-Whelan, A. M., Sipőcz, B., Günther, H., Lim, P., Crawford, S., ... others (2018). The astropy project: building an open-science project and status of the v2. 0 core package. *The Astronomical Journal*, 156(3), 123.
- Burkardt, J. (2014). The truncated normal distribution. *Department of Scientific Computing Website, Florida State University*, 1, 35.
- Coulton, W. R., Armstrong, R., Smith, K. M., Lupton, R. H., & Spergel, D. N. (2018). Exploring the brighter-fatter effect with the hyper suprime-cam. *The Astronomical Journal*, 155(6), 258.
- Downing, M., Baade, D., Sinclair, P., Deiries, S., & Christen, F. (2006). Ccd riddle: a) signal vs time: linear; b) signal vs variance: non-linear. In *High energy, optical, and infrared detectors for astronomy ii* (Vol. 6276, pp. 76–86).
- Harris, C. R., Millman, K. J., Van Der Walt, S. J., Gommers, R., Virtanen, P., Cournapeau, D., ... others (2020). Array programming with numpy. *Nature*, 585(7825), 357–362.
- Ivezić, Ž., Kahn, S. M., Tyson, J. A., Abel, B., Acosta, E., Allsman, R., ... others (2019). Lsst: from science drivers to reference design and anticipated data products. *The Astrophysical Journal*, 873(2), 111.
- Koren, M. (2020). *An influential female astronomer is getting her due*. Retrieved from <https://www.lsst.org/sites/default/files/sites/default/files/docs/Vera%20Rubin%20Well-Deserved%20Space%20Observatory%20-%20The%20Atlantic.pdf>
- Lage, C., Bradshaw, A., & Tyson, J. A. (2017). Measurements and simulations of the brighter-fatter effect in ccd sensors. *Journal of Instrumentation*, 12(03), C03091.
- LSST Science Collaboration, Abell, P. A., Allison, J., Anderson, S. F., Andrew, J. R., Angel, J. R. P., ... et al. (2009, December). LSST Science Book, Version 2.0. *ArXiv e-prints*.
- Lupton, R. H. (2014). Consequences of thick ccds on image processing. *Journal of Instrumentation*, 9(04), C04023.
- Newbry, S., Lange, T., Roodman, A., Reil, K., Bond, T., Rasmussen, A., ... Lee, V. (2018). Lsst camera bench for optical testing: design, assembly, and preliminary testing. In *Ground-based and airborne instrumentation for astronomy vii* (Vol. 10702, pp. 1553–1571).

- NSF. (2020). Nsf-supported observatory renamed for astronomer vera c. rubin. *National Science Foundation*. Retrieved from <https://beta.nsf.gov/news/nsf-supported-observatory-renamed-astronomer-vera>
- O'Connor, P. (2015). Crosstalk in multi-output ccds for lsst. *Journal of Instrumentation*, 10(05), C05010.
- Rubin, V. C. (2011). An interesting voyage. *Annual Review of Astronomy and Astrophysics*, 49, 1–28.
- Snyder, A., Barrau, A., Bradshaw, A., Bowdish, B., Chiang, J., Combet, C., ... others (2020). Laboratory measurements of instrumental signatures of the lsst camera focal plane. In *X-ray, optical, and infrared detectors for astronomy ix* (Vol. 11454, pp. 649–669).
- Walter, C. (2015). The brighter-fatter and other sensor effects in ccd simulations for precision astronomy. *Journal of Instrumentation*, 10(05), C05015.

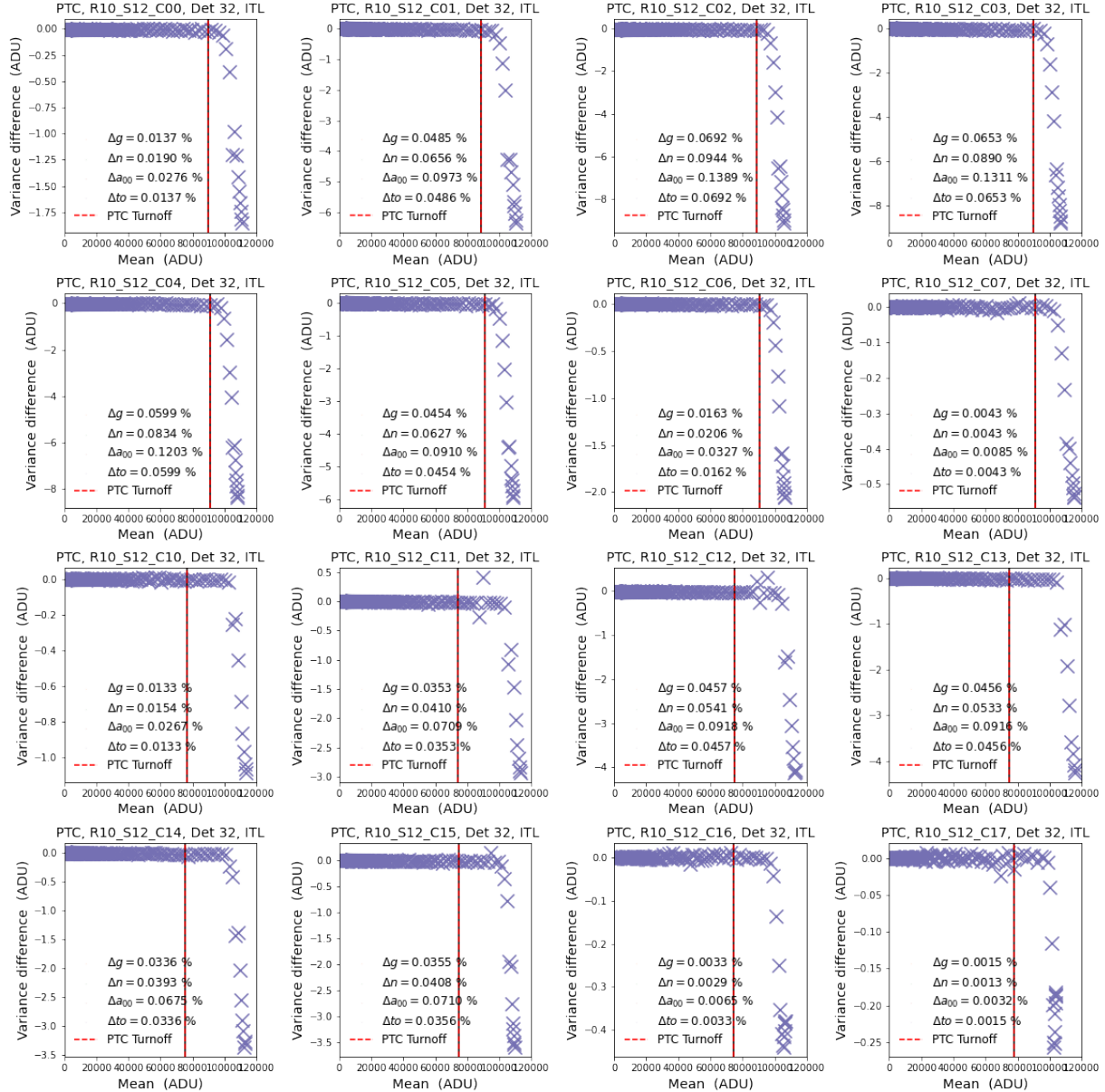


Figure 23: Gráfica de la diferencia de varianza vs la media para el detector 32 (R10_S12) para el fabricante ITL, donde la diferencia de varianza es entre el valor de varianza sin y con corrección por crosstalk. Se muestra esto para cada uno de los segmentos del CCD, mostrando por la línea vertical los valores de PTC-turnoff y en las respectivas leyendas las diferencias entre los parámetros: Δg para la ganancia, Δn para el ruido de lectura, Δa_{00} para el coeficiente del brighter-fatter effect y Δt_o para el PTC-turnoff.

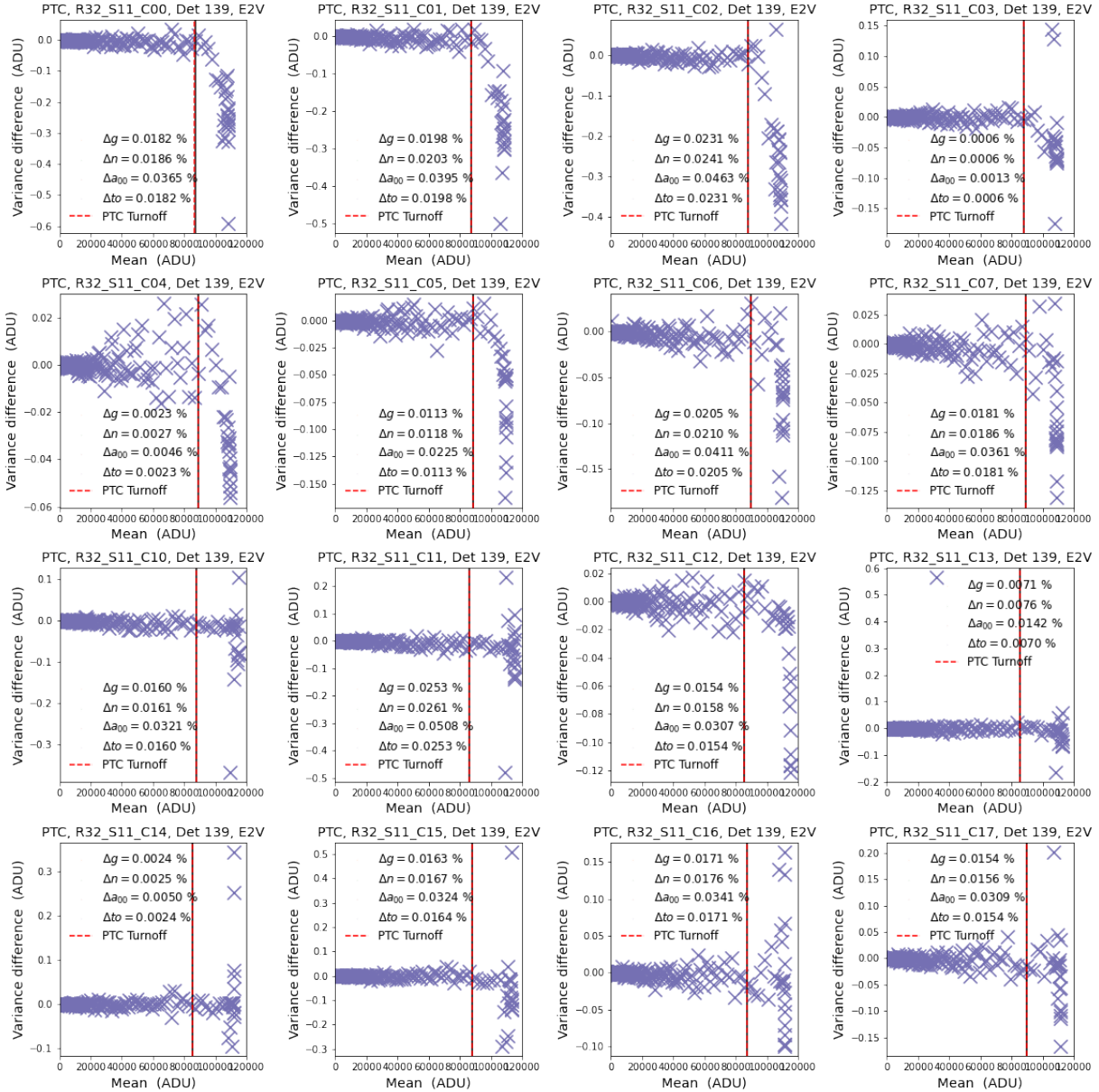


Figure 24: Ver descripción de la figura 23. Esta gráfica es para el detector 139 (R32_S11) para el fabricante E2V.

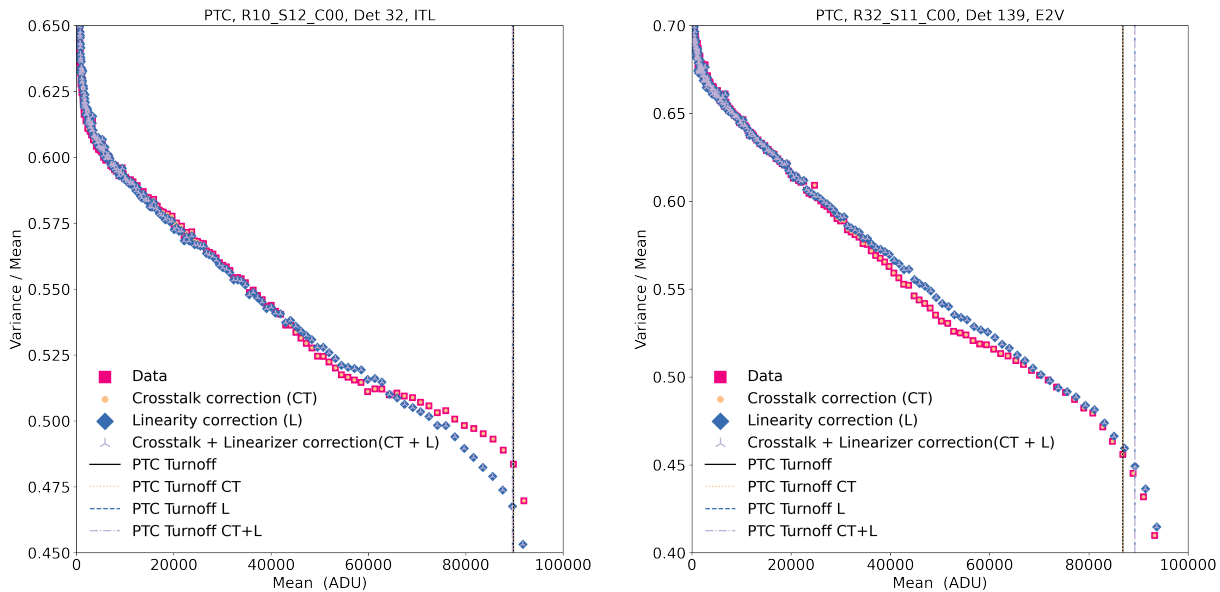


Figure 25: Varianza normalizada por la media vs la media, del detector 32 (R10_S12) para el fabricante ITL, a la izquierda, y para el detector 139 (R32_S11) del fabricante E2V, a la derecha. Se muestra en cuadrados magenta los datos sin corregir por crosstalk (CT) o por la no linealidad, en punto naranja los datos corregidos por CT, por lo diamantes azules los datos corregidos por la no linealidad y por los triángulos los datos corregidos por estos dos efectos: CT y no linealidad. Las líneas verticales representan la ubicación del turnoff.